R76-922241-3

HIGH-POWER INFRARED WAVEGUIDE MODULATORS

SEVENTH SEMI-ANNUAL TECHNICAL REPORT

PERIOD COVERED
25 SEPTEMBER 1975 TO 25 MARCH 1976

CONTRACT NO. N00014-73-C-0087

D D C

JUN 14 1976

D

UNITED TECHNOLOGIES RESEARCH CENTER
EAST HARTFORD, CONNECTICUT 06108

76—03—205—1

UNITED TECHNOLOGIES RESEARCH CENTER

UNITED TECHNOLOGIES™

East Hartford, Connecticut 06108

(14)

UTRC/R76-922241-3

(9) Seventh Semi-Annual Technical Report, no. 7, Sep 75-Mar 76,

(6) High-Power Infrared Waveguide Modulators,

By

(10) P. K. Cheo, D. Fradin, M. Gilden and R. Wagner
United Technologies Research Center
East Hartford, Connecticut 06108

(11) 30 Mar 76   (12) 70p.

Principal Investigator - P. K. Cheo (203) 565-4297

Prepared for the (15) Office of Naval Research
Contracting Officer: Dr. M. White ARPA order-1860
Contract No. N00014-73-C-0087,
Contractor Modification No. P00008 $438,488
25 August 1972 to 25 October 1976

Sponsored By

DDC
RECEIVED
JUN 14 1976
D

409252

TABLE OF CONTENTS

TABLE OF CONTENTS (Cont'd.)

1.0 TECHNICAL REPORT SUMMARY

1.1 Program Objectives

The objective of this program is to develop an efficient and reliable ultra-wideband waveguide modulator for CO_2 lasers that will be useful for high resolution, imaging optical radars and high-data-rate optical communication systems. Efficiency and reliability are obtainable by using integrated optics technology.

During this reporting period (September 1975 to March 1976), major objectives are (1) to obtain the sideband power at a frequency 16 GHz offset from a CO_2 laser V-R transition greater than 10 mW, (2) to obtain a modulation bandwidth exceeding 500 MHz, (3) to obtain a good transmitted optical beam quality, and (4) to establish an optimum waveguide modulator configuration and define the operational capabilities and limitations of this modulator. These research and development efforts are essential for making an accurate assessment of active infrared waveguide devices that shall lead to a rational decision regarding the advisability of initiating a high-power infrared waveguide modulator brassboard development program.

1.2 Major Accomplishments

During the reporting period, we have accomplished all above objectives. Specifically, we have obtained the following results: (1) the sideband power of 40 mW at 16 GHz was obtained by using a 15 watts CO_2 laser and a 22 watts Ku-band microwave driver as the inputs to a 25 μm thick GaAs waveguide, (2) the measured modulation bandwidth exceeds 1 GHz, (3) the transmitted beam shape was almost Gaussian, and, finally (4) an optimum waveguide configuration has been established. It consists of a slowly tapered raised-ridge structure, which shall provide the highest sideband conversion efficiency, the desired beam quality and power handling capability.

To accomplish the first objective, we have made considerable improvements in both the waveguide structure and optical coupling technique. These improvements have yielded the highest optical coupling efficiencies of 72 percent and 100 percent for the input and output coupler, respectively. With water cooling, one of these modulators (LD-4) has been tested at MIT Lincoln Laboratory with a high-power microwave TWT driver up to 80 watts. This modulator has subsequently been optically evaluated at our Laboratory and has yielded no discernable change either in its optical characteristics or in its ability to generate sideband power. To achieve good transmitted beam quality, a two-dimensional waveguide in a channel configuration has been used to confine the guided-wave mode within a narrow and long electro-active region. Without the channel, the microstrip electrode distorts the propagating wave by spreading the beam in the plane of the guide.

1.3 Future Work

Work is in progress to generate higher sideband power in the range from 100 mW to 200 mW. In parallel, work is in progress to develop a technique that shall filter out a single sideband with a relatively broad passband of $\gtrsim$ 1 GHz from the modulator output. Experimental investigation of the slowly tapered raised-ridge waveguide structure will also be carried out.

2.0 INTRODUCTION

Either epitaxially grown, (Refs. 1, 2, 3) or mechanically polished (Refs. 4, 5) infrared waveguides have been investigated extensively at only very low optical power levels. As optical input power and/or electrical driving power to these waveguide devices is increased, waveguide imperfections associated with free carrier absorption, lattice mismatch, dislocation, process-induced damage, thickness uniformity, and most importantly, electric power loss at high frequencies, surface deformation by electrodes and stress-induced birefringence can severely degrade the performance of these waveguide devices from their idealized situations.

In this program we have explored several waveguide structures that may be suitable for high-power laser systems applications. Of particular interest is the device performance of wideband electro-optic modulation of a high-power CO_2 laser beam. For a high resolution optical imaging radar system, where modulation bandwidth far exceeds one GHz, the selected approach is to generate a single sideband power from a CO_2 laser carrier at microwave frequencies. In this case, broadband modulation can be obtained by sweeping the microwave frequency over a range of several GHz. This has been demonstrated (Ref. 6) by interfacing a high-power infrared waveguide with a microwave microstrip transmission line.

This report describes an infrared waveguide modulator suitable for use with high power CO_2 laser (> 10 watts) and high power microwave source ($\simeq$ 100 watts). The fabrication techniques and some preliminary optical characteristics of a bonded-down GaAs thin-slab waveguide have been already detailed in the 6th Semi-Annual Report (Ref. 7). Because of microwave propagation loss, the electrodes must be made of copper and must be in a close contact with the waveguiding layer for efficient interaction. This rules out the use of epitaxial waveguide structures and limits the choice to the thin dielectric slab waveguide configuration. The top electrode must be in the form of a very long and narrow stripline in order to provide the desired sideband conversion efficiency and the bandwidth. This requirement causes difficulty in beam alignment with respect to the electrode. We often observed that a slight misalignment of the laser beam can produce tremendous distortion of the output laser beam shape by spreading and deflecting the beam in the plane of the waveguide. This lens-like effect during the quiescent phase is caused by the waveguide surface deformation along the edges of the electrode, that produces a localized stress-induced birefringence which, in our case, is about two orders of magnitude larger than the field-induced birefringence via the electro-optic property of the waveguide. Beam distortion is further enhanced when microwave power is applied to the modulator. Beam distortion can be eliminated by using a wider electrode so that along the entire propagating path laser beam is confined within the electrode region. Under this condition we observed no beam distortion either with or without the microwave field. Certainly widening of the electrode is not desirable because it reduces both the conversion efficiency and the modulation

bandwidth. To confine a laser beam within a narrow path over a long distance, one alternative way is to compensate this lens-like effect by using a two-dimensional channel waveguide which can be made by removing a small amount of material along the edges of the microstrip electrode. In this way we have obtained perfect alignment of the optical beam with microwave field along a narrow (1 mm wide x 2.8 cm long) microstrip electrode without apparent beam distortion.

Previous studies (Refs. 7, 8) indicated that optical transmission through the waveguide by using prism as couplers is about ten times that of grating couplers. This large difference in the relative merits of the two types of couplers is basically caused by two factors, namely the coupling strength and partition of energy. Because grating is an inherently weak coupler, larger coupling length than that of a prism is required for efficient energy transfer. For this reason waveguide structural imperfections have much greater effect on the grating coupler. Chapter 3.0 gives a detailed discussion on these effects.

Chapter 4.0 gives a detailed processing procedure for waveguide fabrication. To make the report self-consistent, this chapter gives a brief review of the processing techniques and elaborates on those which are developed during this reporting period. Specifically, the noncontracting thickness measuring techniques with an accuracy to better than 0.1 μm has been used to improve the thickness tolerance of our bonded-down thin-slab waveguides.

Chapter 5.0 discusses the microwave characteristics of the waveguide modulator. Special emphasis is given to the understanding of the modulator bandwidth which is a trade-off parameter for a resonator-type of modulator design.

Chapter 6.0 presents both the optical transmission data and microwave modulation data. Optical measurements include the coupling efficiency, power loss in the top and bottom electrodes, and optical confinement characteristics with a channel wave-guide. Also included are measurements of sideband power conversion efficiency and modulation bandwidth.

The last chapter (7.0) is a preliminary investigation of an optimum waveguide modulator configuration. Calculated results for the performance of such a modulator structure are given.

2.1 References

1. Cheo, P. K., J. M. Berak, W. Oshinsky, and J. L. Swindal, Appl. Optics 12, 500 (1973).

2. Chang, M. S., W. S. C. Chang, B. L. Sopori, H. R. Vann, M. W. Muller, M. G. Craford, D. Finn, W. O. Groves and A. H. Herzog, Appl. Optics 14, 1572 (1975).

3. Spears, D. L., A. J. Strauss, S. R. Chinn, I. Melngailis, and P. Vohl, Integrated Optics Tech. Digest, January 12-14, 1976, Paper TuD3.

4. Anderson, D. B., and J. T. Boyd, Appl. Phys. Lett., 19, 266 (1970).

5. Lotspeich, J. F., Appl. Optics 13, 2529 (1974).

6. Cheo, P. K., and M. Gilden, Appl. Phys. Lett., (May 1976).

7. Cheo, P. K., M. Gilden, and R. Wagner: Infrared Waveguide Modulators at Microwave Frequencies, 6th Semi-Annual Tech. Rept., Contr. No. N00014-73-C-0087, September 1975.

8. Cheo, P. K., D. Fradin and R. Wagner: Microwave Waveguide Modulators for CO_2 Lasers, 5th Semi-Annual Tech. Rept., Contr. No. N00014-73-C-0087, March 1975.

3.0   TIVE MERITS OF INTEGRATED-OPTIC COUPLERS

3.1 Introduction

The extensive data on grating and prism couplers reported in the previous two semiannual reports (Refs. 1, 2) indicate that (1) the measured performance characteristics of our couplers deviate substantially from the characteristics of ideal grating structures, (2) the prism performance characteristics correlate well with the characteristics of ideal prism couplers, (3) substantially higher total coupling efficiencies are normally achieved with the prism coupler. In Ref. 1 it was suggested that waveguide thickness variations may play an important role in the grating chracteristics, and selected data on transverse beam deflection within the waveguide was presented to demonstrate that significant waveguide thickness variations were often present in the available waveguides. Nonetheless, the theoretical considerations introduced in Ref. 1 (Section 3) were not developed sufficiently to explain the details of the experimental data. A particularly confusing observation was that, when both a prism coupler and a grating coupler were used on the same waveguide, use of the prism resulted in substantially better performance. (See Fig. 1 of Ref. 2). If waveguide thickness variations strongly affected the grating performance, it was difficult to understand why performance with the prism coupler was not similarly degraded.

In this section we show that the major trends of the experimental data can, in fact, be explained by assuming that small but significant thickness variations were present in the waveguides used in our earlier experiments. In addition to explaining the major features of the experimental data, this analysis provides both guidance on the choice of couplers in various waveguide configurations and information that can be used to establish waveguide thickness tolerances.

The theoretical calculations were conducted in collaboration with Dr. S. T. Peng and Prof. T. Tamir of Polytechnic in Ref. 3. Except for calculations based on the overlap integral discussed in Ref. 1, the calculations reported in this section were performed at the Polytechnic computer facilities.

In Section 3.2 the important results of the theoretical analysis are summarized. Comparison to experimental data is made in Section 3 3. It is concluded that waveguide thickness variations dominate the grating performance, because for our configuration the grating coupler is a weak coupler. Large-area input laser beams, whose areas exceed the areas over which the waveguide is acceptably flat, are needed for aperture matching. As a result, aperture matching cannot be achieved with our grating structures. Proper use of a prism coupler with our waveguides, on the other hand, results in values of the coupler parameter α that are sufficiently large so that aperture matching can be achieved with relatively small-area laser beams. Over small areas the waveguides are generally sufficiently flat so that thickness variations do not strongly affect the coupling efficiency.

3.2 Theoretical Considerations

3.2.1 General Coupler Characteristics

The general conditions that lead to a loss in input coupling efficiency are discussed in this section. Particular attention is given to the importance of phase-matching. In addition, the far-field intensity distribution for the output from a perfect coupler is derived. By comparing this ideal distribution to measured distributions, we obtain additional indications that the structure of this coupling region is generally imperfect even when prism couplers are used with the bonded waveguides and nearly optimum coupling efficiencies are measured.

The grating or prism coupler provides a mechanism for the exchange of energy between a free-space mode and a guided mode of the waveguide. As discussed in previous reports, the prism creates mode coupling by the process of frustrated total internal reflection and the grating creates coupling by a complex diffraction process. Despite the differences in their operation, the two couplers are very similar in their general characteristics. This similarity is a consequence of the fact that both couplers perturb the guided modes of the waveguide structure to produce "leaky" waves that are characterized by a complex propagation constant with an imaginary part, α (Ref. 4).

The exchange of energy between the two modes is a coupled-mode process, with the fraction of energy that is transferred dependent upon both amplitude matching and phase matching. In the conventional coupled-mode problem (Ref. 5), maximum energy exchange occurs when the interaction length is approximately equal to some characteristic length (amplitude matching) and when the phase velocities of the two modes are equal (phase matching). In all cases of interest, phase matching is the more important constraint. The grating and prism equations are the conditions for perfect phase matching; the form factor in Eq. (6) of Ref. 1 (p. 17) expresses the consequences of deviations from perfect amplitude matching.

Consider, first, the amplitude matching condition. As illustrated in Fig. 3.1, the beam I is incident on the coupler at the phase-matched angle (θ_G for the grating and θ_P for the prism). It was shown in Ref. 1 that for a uniform input beam, the input coupling efficiency η is

$$\eta = f \, \frac{1}{\alpha R} \, [1 - \exp{(-2\alpha R)}]^2 \tag{1}$$

where $f = 1$ for a prism coupler (assuming no scattering losses); $f < 1$ for a grating coupler (accounts for energy loss to transmitted beam T and to scattering); α is

the coupling or leaky-wave parameter; and 2R is the incident beam diameter. Equation (1), which is plotted for f = 1 in Fig. 3.2, varies linearly with αR for small αR and has a broad maximum at αR = 0.65.* When the beam radius is adjusted so that R = 0.65/α, η = 0.81f. At all other values of R, η < 0.81f and the beam is not properly phase-matched.

The effects of deviations from perfect phase matching were analyzed in Ref. 1 (p. 18) for a uniform input beam. If the input beam is incident on the coupler at an angle θ_G (or θ_p) = θ_0 + $\Delta\theta$, where θ_0 satisfies the grating (or prism) equation and $\Delta\theta \neq 0$ is the error in incident angle, then the incident beam is no longer perfectly phase-matched. The coupling efficiency will be less than its optimum. Using an overlap integral calculation, η was shown in Ref. 2 to be

$$\eta = f \frac{\alpha R}{(\alpha R)^2 + (aR)^2} \quad (1 + e^{-4\alpha R} - 2e^{-2\alpha R} \cos 2aR) \qquad (2)$$

where a = $(2\pi/\lambda)$ $(\cos \theta_0)$ $\Delta\theta$. It is easily seen that η is a function of the scaling parameter $\gamma'' = \pi$ (R $\cos \theta_0/\lambda)\Delta\theta$, where $\Delta\theta$ is expressed in radians. This characteristic scaling was first noted by Tamir and Bertoni (Ref. 6) who performed a similar calculation of η for a Gaussian input beam. Equation (2) is plotted in Fig. 3.3 as a function of γ'' under the assumption that αR = 0.65. For reference, the corresponding values of $\Delta\theta$ are also shown for the specific condition R $\cos \theta_0$ = 1.55 mm.

Figure 3.3 shows that the input coupling efficiency is reduced to about half its peak value when $\gamma'' \approx 0.5$. The acceptance half-angle of the generalized coupler is thus

$$\Delta\theta_c \text{ (radians)} \cong \frac{\lambda}{2\pi} \frac{1}{R \cos \theta_0} \qquad (3a)$$

for a uniform beam. When a Gaussian beam that has a radius w (1/e in amplitude) is incident on the waveguide, Eq. (3a) is replaced by (Ref. 6)

$$\Delta\theta \text{ (radians)} \cong \frac{\lambda}{\pi} \frac{1}{w} . \qquad (3b)$$

Note that the Gaussian radius in the plane of the waveguide is w/$\cos \theta_0$. Equation (3) is used in the next section to calculate the effect on η of a thickness taper in the coupling region.

---

* For a Gaussian beam, the shape of η is slightly changed. A maximum value of 0.80 f occurs at αR = 0.68.

The total coupling efficiency, $\eta_{t\ell}$, will be proportional to η. Additional factors that reduce $\eta_{t\ell}$ are propagation losses in the waveguide, partition of energy into multiple beams at the output (for the grating), and losses due to the limited length, ℓ_c, of the coupling region. The last effect introduces a factor of $[1 - \exp(-2\alpha\ell_c)]$ as noted in Section 3.4.

Equations (1) and (2) are obtained by calculating the overlap between the uniform input field and a normalized aperture field E_a where

$$E_a = \exp(-\alpha x) \tag{4}$$

and x is the coordinate that is oriented along the waveguide in the direction of beam propagation. If the coupler is used to couple light out of the waveguide, then the output beam has the form of Eq. (4) immediately above the coupler (Ref. 1). When the coupler is uniform, α is a constant and E_a is peaked at the inside edge of the grating. Because the output beam has a planar phase front, the far-field distribution is symmetric as we now show.

Assume for simplicity that θ_G (or θ_p) = 0. The far-field distribution $E(\phi)$, at a distance z' from the waveguide, is proportional to the one-dimensional Fourier transform of E_a. If x' is the coordinate in the far-field observation plane that is parallel to the x-axis, then $\tan\phi = x'/z'$. Since the output field is a beam with a low angular divergence, $\tan\phi \approx \phi$ and the paraxial ray approximation is valid. $E(\phi)$ is given by

$$E(\phi) = A\int_0^\infty e^{-\alpha x} e^{ik\phi x} dx \tag{5}$$

where A is a complex constant that absorbs the phase terms. Evaluating Eq. (5) and calculating the light intensity I gives

$$I \propto E(\phi) E^*(\phi) = \frac{A^2}{\alpha^2 + k^2\phi^2} . \tag{6}$$

If θ_G or $(\theta_p) \neq 0$, then a linear phase term equal to $2\pi/\lambda (\sin\theta)x$ is introduced into the integral in Eq. (5). This change has the effect of rotating the observation direction without changing the form of Eq. (6).

Equation (6) shows that the far-field-distribution of the light coupled from either a grating or a prism coupler is symmetric with respect to ϕ. It can be shown from the general form of the Fraunhofer integral, in fact, that if α varies with x along the grating, the exact form of I will be somewhat changed but I will still be symmetric with respect to ϕ. The symmetry is only destroyed when the aperture function E_a has a nonplanar phase front. If a measurement of I indicates asymmetry,

therefore, the phase surface of the aperture function is nonplanar. As discussed later, this effect can occur when the waveguide thickness in the coupling region is not uniform. Asymmetry in the far field has been observed even with the bonded waveguides and prism couplers used in our most recent work (see Figs. 7 and 8 in Ref. 2).

3.2.2 Waveguide Thickness Variations

As the waveguide thickness, t_w, in the coupling region varies, three effects occur. First, the coupling angle changes; second, the strength of the coupling changes; third, for the grating, the value of f in Eqs. (1) and (2) changes. Each of these effects and their impact on coupling efficiency are considered in this section.

Coupling angle changes are the result of changes in the waveguide effective index-of-refraction, $n_{eff} = \beta/k$. If t_w varies in the coupling region, then n_{eff} also varies spatially. The coupling angle $(\Delta\theta = 0)$ is related to n_{eff} by either the relationship

$$\theta_G = \text{arc } \sin(\lambda/\Lambda - n_{eff}) \tag{7a}$$

or the prism coupler equation

$$\theta_p = \frac{\pi}{4} + \text{arc } \sin \left\{ n_2 \sin \left\lfloor \text{arc } \sin \left(\frac{n_{eff}}{n_p} - \frac{\pi}{4} \right) \right\rfloor \right\} \tag{7b}$$

where Λ is the grating periodicity; n_p is the prism index-of-refraction; and the prism entrance face is assumed to be inclined at an angle of $\pi/4$ relative to the plane of the waveguide. From these relationships, it is apparent that spatial variations in t_w lead to spatial variations in the coupling angle.

The relationship between θ_G and waveguide thickness was derived in Ref. 1 using both the unperturbed waveguide dispersion relationships to obtain n_{eff} and Eq. (7a) with $\lambda/\Lambda = 3.855$ to obtain θ_G. Figure 6 of Ref. 1, which is reproduced here as Fig. 3.4, shows the result of that calculation. Similar results are obtained for θ_p. It is seen that the variation of θ_G with t_w is strongly mode-dependent.

As discussed in Ref. 1, thickness variations in the coupling regions cause the input coupling efficiency to decrease for the following reasons: when thickness variations exist, the coupling angle varies across the irradiated region of the coupler. Since the input beam is generally incident at a single angle (planar phase front) there will be an angular error $\Delta\theta$ that varies spatially across the beam. To a good approximation, the regions where $\Delta\theta$ exceeds the value given by Eq. (3), there is no coupling. A linear taper can thus cause a significant degradation in the coupling efficiency. This degradation can be especially serious for

the higher-order modes, because as indicated by Fig. 3.4, the sensitivity of coupling angle to t_w increases rapidly with mode-number.

Figure 3.5 shows how the coupling efficiency drops for the TE$_4$ mode with increasing thickness taper. This calculation, which was obtained by Peng and Tamir in Ref. 3, uses parameters that are appropriate to the grating couplers studied in Ref. 1. The efficiency in Fig. 3.5 must be multipled by the factor f as in Eq. (1) in order to determine the actual coupling efficiency. The TE$_4$ mode was chosen for evaluation, because calculations indicated that it was aperture-matched for a 1 mm input Gaussian beam.

The most striking feature of the curve in Fig. 3.5 is that modest thickness tapers cause significant reductions in coupling efficiency. As discussed later, experimentally observed thickness variations are generally 0.5 to 1.0 μ/mm in our best free-standing waveguides so that the TE$_4$ mode cannot be efficiently excited in them. The loss in efficiency caused by a given taper is less for the modes of order lower than 4. As discussed below, however, the lowest order modes cannot be experimentally aperture-matched when a grating is used. In such cases, the input efficiency will be less than 0.80 f at zero taper.

Thickness variations change the value of α. For a prism coupler, a closed form expression for α can be found. This relationship can be found on p. 2-9 of Ref. 2. For the grating coupler α must be calculated numerically. Although several groups have calculated α using perturbation models, the Polytechnic Group (Ref. 7) has developed both the most accurate perturbation model and the only rigorous theory for grating couplers.

Calculations of α have been conducted both for the prism coupler assuming a gap spacing of 0.1 μ (a value that was inferred from measurements reported in Ref. 2, p. 2-10) and for the grating coupler using the Polytechnic perturbation model. Figures 3.6 and 3.7 summarize the results. Several important features are apparent from these results. These features include:

(1) For the prism, α decreases monotomically with t_G but increases with mode number

(2) For the grating, the same average trends are observed but a strong oscillation is superimposed on α. This oscillation, which is the result of interferences between reflections from the two waveguide boundaries, is especially pronounced because of the large index difference between the waveguide and the air. Variations in α for the grating by a factor of about 3 are predicted for thickness variations as small as 0.3 μ.

(3) α for the prism is typically more than an order-of-magnitude larger than α for the grating for the same t_G and mode number. For the TE$_1$ mode and $t_G = 25$ μ, for example, $\alpha(\text{prism}) \simeq 0.8 \times 10^{-3} \mu^{-1}$ and $\alpha(\text{grating}) \simeq 3 \times 10^{-5} \mu^{-1}$.

Because α varies with t_G, the coupling efficiency η may be measurably altered by thickness variations. Both the magnitude and the sign of the effect depend on the details of the thickness variations. If the thickness variations are such that α is less at the inside edge of the coupler, for example, then the peak of the aperture function, E_a, will be shifted towards the center of the coupler. In such a case, E_a will have a closer match with the actual input beam distribution, and η will increase. If α is greater on the inside edge of the coupler, on the other hand, η will decrease. In general, the effects of spatial variations in α on the coupling process will be much less important than the effects of spatial variations in the coupling angle. This last fact, which can be demonstrated quantitatively with an overlap integral calculation, is a direct consequence of the relative insensitivity of coupled-mode processes to amplitude matching.

The magnitudes of α predicted by theory are much more important to the present coupling problem than the detailed variation of α with t_G. As already noted, optimum coupling occurs when $\alpha R = 0.65$ for a uniform beam. Using the calculated value of α cited above, we find that for TE_1 the optimum input beam diameters (projected into the plane parallel to the waveguide) are about 1.6 mm for the prism and 43 mm for the grating. It is clear that aperture-matching can be achieved with the prism coupler, but that aperture matching is not practical with the grating. In fact, input beam diameters greater than about 2.5 mm are impractical with the available waveguides, because thickness variations due to rounding at the waveguide edges become severe over such distances.

A third consequence of thickness variations is that the factor f in Eqs. (1) and (2) will vary across the grating coupler. (Recall $f = 1$ for a prism, because there is no transmitted beam at the input.) This effect does not seriously degrade the coupling efficiency, but it can significantly change the intensity distribution observed when the coupler is used to couple light out of the waveguide.

Peng and Tamir (Ref. 3) have calculated f for an output grating. In the special case of ideal aperture-matching and no scattering, their calculated function and f in Eq. (1) are the same. This calculation, which is based on a perturbation analysis, predicts that f will depend strongly on t_G as shown in Fig. 3.8. If thickness tapers of the order of $1\mu/mm$ are present, the large oscillations in f shown in Fig. 3.8 will cause the output intensity distribution observed just above the output grating to depart from the ideal exponential form. Such departure from the ideal form is, in fact, frequently observed with our grating couplers, as noted in the next section.

3.3 Experimental Results

The experimental techniques and representative data on both prism and grating couplers are described in Refs. 1 and 2. In this section we summarize the important aspects of the data.

Table 3.1 summarizes the performance characteristics of a free-standing waveguide (sample B-8) with grating couplers. These data, which were taken from Ref. 1 (p. 28), indicate (1) low total coupling efficiencies, (2) low input coupling efficiency for TE_2, and (3) significant discrepancies between those incident beam diameters (projected into the waveguide plane) that gave maximum coupling efficiencies and the diameters calculated assuming aperture-matching. In addition, the near-field and far-field intensity distributions of the output beams usually did not resemble the characteristic distributions expected for an ideal coupler. Figure 3.9, for example, illustrates the shape of the beam coupled from the TE_2 mode at sample B-8 as measured approximately 400 μ from the grating surface. In this region the output from a perfect uniform coupler will approximately match an exponential function with a slightly rounded leading edge. In the far-field, the measured beams did not have the symmetric shape characteristics of the output of an ideal coupler. In general, therefore, the performance of the grating couplers did not correlate with the predicted performance of uniform grating structures.

In contrast, the performance of the prism couplers indicated reasonable correlation with the theory of uniform structures. For example, an input coupling efficiency of 72 percent was observed with a prism coupler when a Gaussian beam having a 1 mm diameter ($1/e^2$ - intensity points) was used at the input. For this waveguide, both the coupling efficiency and the optimum beam diameter were within about 10 percent and 30 percent, respectively, of theoretical values. The coupling efficiencies measured for the other modes and with other prism/waveguide combinations, though less than the best-case value cited here, were always much closer to theoretical predictions than were efficiencies measured for grating couplers. In general, the coupling efficiencies and optimum input beam diameters for the prism couplers used with both the freestanding and the bonded waveguides were in reasonable agreement with the theory.

Other data taken with prism couplers, however, indicated that structural imperfections in the coupling region were present with both the freestanding and the bonded waveguides even though, in the best cases, these imperfections appeared to have little effect on the coupler performance. As discussed in Ref. 2, for example, the output beams were typically steered in the plane of the waveguide and the far-field intensity distributions of the output beams were generally somewhat asymmetric (see pp. 2-16 and 2-17 in Ref. 2). The beam steering was interpreted in Ref. 1 to be the consequence of waveguide thickness tapers transverse to the propagation direction, and the asymmetry in the far-field was interpreted in Section 3.2.2 of this report to be the consequence of thickness variations in the coupling region. Nevertheless performance of the prism coupler was not

TABLE 3.1

Performance of a Free-Standing Waveguide With Grating Couplers
(Sample 3-8)

Grating periodicity, μ	2.75
Groove depth, μ	2.0
Waveguide thickness, μ	24
Propagation path, cm	1.3
Thickness taper, μ/mm	
transverse	0.6 ± 0.2
longitudinal	0.5 ± 0.2

Coupling Angle	Mode	η_{total}, %	$2R_{opt}$, mm Experimental	Theoretical
35.6	TE_0	0.3	≥ 3.0	124
37.8	TE_1	2.4	2.5	31.3
40.2	TE_2	4.6*	2.0 to 2.5	14.4
43.8	TE_3	4.3	1.4 to 2.1	8.4
48.8	TE_4	2.1	≤ 1.4	5.2

* The input coupling efficiency, as determined by a dip in the sum of
the transmitted and reflected beams, was 12 percent for this mode.
Input beam was nearly uniform.

severely limited by imperfections of waveguide. Direct comparisons between a grating coupler and a prism coupler on a single waveguide (Ref. 2, pp. 2-2) which indicated superior performance by the prism, support this conclusion.

Poor performance of gratings was not caused by the quality of grooves of the gratings. To verify this, each grating was subjected to careful visual inspection under an optical microscope. In some cases, electron microscope photographs were made of the gratings in profile. It was found that, except for isolated defects, the gratings were remarkably uniform. In addition, x-ray diffraction tests conducted for us by IBM indicated that the grating regions were effectively strain-free. The only important structural defect that was always present in the coupling regions were waveguide thickness variations. Microscopic inspection of cleaved samples indicated that average thickness tapers of about 0.5 μ/mm were present in the best free-standing waveguide structures, and tapers of more than 2 μ/mm were present in the worst samples tested. Best grating coupler performance was always obtained with the most uniform waveguides.

The available data thus indicate that for the over-moded waveguides used in the thin-film modulator, the prism coupler is preferred. The relatively poor performance of the grating coupler is shown in the next section to be related to the inherently weak coupling characteristic of the grating for our waveguide structures.

3.4 Discussion and Conclusions

It is now clear that waveguide thickness variations alone can account for the poor performance of the grating structures. Although such variations were generally also present in the prism coupler experiments, the analysis discussed in Section 3.2 provides, as we now show, a natural explanation for the superior performance of the prism coupler with our thin-slab waveguide structures.

Significant variations of t_G within the input coupling region cause the coupling efficiency to decrease, because thickness variations prevent the input beam, which typically has planar phase surfaces, from being properly phase-matched across the entire beam cross-section. In effect, the light rays enter the coupler as a collimated bundle at a single angle with respect to the waveguide normal. Thickness variations cause the coupling angle of the grating to vary spatially, however, and when the incident ray angle deviates too far from the coupling angle appropriate to a particular region of the coupler, then no light will be coupled into the waveguide through that region. If the beam diameter needed to aperture-match exceeds the spatial extent, X_f, of this acceptably flat region, then the beam cannot be aperture-matched. In this case, the coupling efficiency will be lower than peak theoretical values, and the beam diameter that leads to maximum coupling will be nearly X_f insteady of $1.3/\alpha$ as predicted by the theory of uniform couplers.

As discussed in Section 3.2.2 the effect of waveguide thickness variations on the coupling efficiency is strongly mode-dependent so that X_f will be mode-dependent. The TE_0 mode, for example, which propagates in our structures almost as a bulk wave (cf. Fig. 3.4), is little affected by variations in t_G. As a consequence, X_f (TE_0) will be relatively large. For the grating coupler, X_f (TE_0) significantly exceeds the coupler size. Values of X_f for the higher order modes were generally less than both the coupler size and the aperture-matched beam diameters so that the beam diameters that produced the highest coupling efficiency (see Table 3.1) were measures of X_f.

In general, then, $X_f < 1.3/\alpha$ for the grating coupler so that thickness variations strongly affected the grating performance. The prism is an inherently stronger coupler, however, and generally $X_f \gtrsim 1.3/\alpha$ for the waveguides tested. As a consequence, the input beam could usually be aperture-matched with the lower-order modes and near-optimum input efficiencies obtained. In our application, the prism coupler is the preferred choice primarily because it is a stronger coupler than the grating.

A simple calculation illustrates how the limits imposed by coupler uniformity and coupler size prevented good grating performance. Consider the TE_2 mode in Table 3.1. For this mode, the measured optimum beam diameter was 2 to 2.5 mm, and the theoretical diameter for aperture-matching was 14.4 mm. Hence, $\alpha R = 0.09$ to 0.11 for this mode instead of the optimum value of 0.65. From Eq. (1), the calculated input efficiency is $\eta = 0.30f$ to $0.36f$. Experimentally, 36 percent of the incident energy was transmitted and 10 percent of the incident energy was lost to scattering so that $f = 0.54$ and $\eta = 0.16$ to 0.19. This efficiency compares reasonably well to the measured value of 0.12 ± 0.03. The total coupling efficiency $\eta_{t\ell}$ for this mode should have been

$$\eta_{t\ell} = \eta(1-e^{-2\alpha\ell_c})e^{-\sigma L} f_o \qquad (8)$$

where ℓ_c is the output coupler length (3 mm); $e^{-\sigma L}$ is the propagation loss between the two couplers; and f_o is the fraction of outcoupled energy in the upper beam (0.65).* Using the theoretical value of $\alpha = 9.0 \times 10^{-2}$ mm^{-1} and $\eta = 0.16$, we find $\eta_{t\ell} = 0.0434 \exp(-\sigma L)$. If the propagation loss due to GaAs absorption is negligible ($\sigma L \ll 1$) as indicated by recent studies, then the theoretical value of $\eta_{t\ell}$ and the experimentally determined value are in nearly perfect agreement. The low coupling efficiencies were thus the consequence of the low values of α produced by the grating with our waveguide structures. Because α values were small, aperture matching at the input was not possible and the grating output coupler was not long enough to couple all of the guided light out of the waveguide.

_____

* This is a theoretical value. The true value could not be accurately determined because of experimental difficulties.

Substantially higher coupling efficiencies could be obtained by thinning the waveguide to increase α. Calculations by Peng and Tamir indicate, for example, that the TE_0 mode could be aperture-matched with a 2 mm input beam if the waveguide thickness were tapered to 8.1 μ in the coupling regions with 2 μ grating grooves etched into the waveguide. In this arrangement, the output grating would couple virtually all the light out of the waveguide and $\eta_{t\ell}$ would be $ff_0(0.81) = 0.28$. Further increases in η could be achieved, in principle, by increasing f and f_0 by either blazing the grooves (Ref. 7) or carefully controlling the waveguide thickness to influence the partition of energy as in Fig. 3.8.

Improvements in grating performance are possible by further advancing waveguide fabrication techniques. At this time, however, it does not appear that the grating will be useful with the thin-slab modulator.

The theoretical analysis developed in Section 3.2 offers an explanation for the poor coupling efficiencies of the grating couplers. This analysis also provides qualitative explanations for the nonideal output beam distributions observed with both the prism and grating coupler. Thickness variations in the output coupler cause near-field phase distortions in the output beam (changes in ray angle). These distortions were transformed in the far-field to asymmetries in the intensity distributions. For the case of the grating coupler, the near-field amplitude distribution was also affected, because the partition of energy between the upper and lower outcoupled beams is a sensitive function of t_G. Quantitative comparisons between experimental and theoretical intensity distributions cannot be made because a detailed mapping of the spatial variations in t_G was not possible with available techniques.
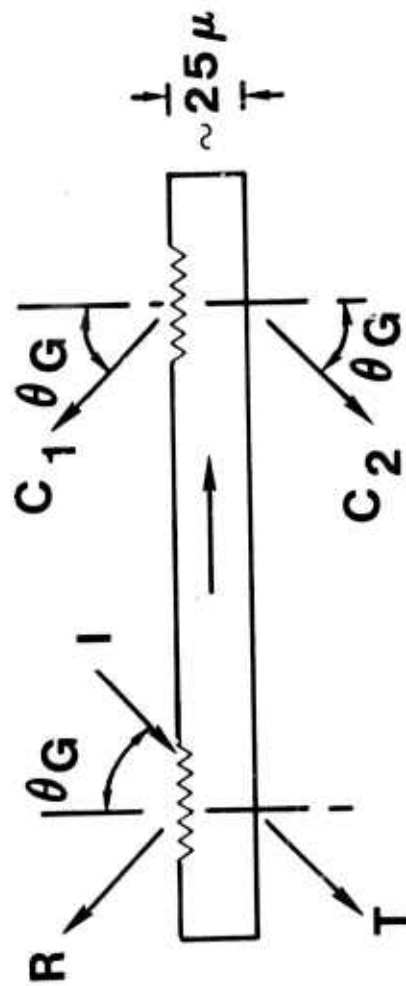
It is thus seen that for the thin-slab waveguide structures, the prism is the preferred coupler both because energy losses to extra beams are eliminated and because the prism is an inherently stronger coupler. Strong coupling permits the excitation of the lower-order modes with small-diameter input beams and thereby largely circumvents the deleterious effects of waveguide thickness variations. The grating coupler is only useful for asymmetric waveguides that are single-mode or nearly single-mode.

The present study has provided a meaningful interpretation of the data accumulated on the grating coupler. It has, in addition, provided the first study of the effects of imperfections on the performance of integrated optics structures.
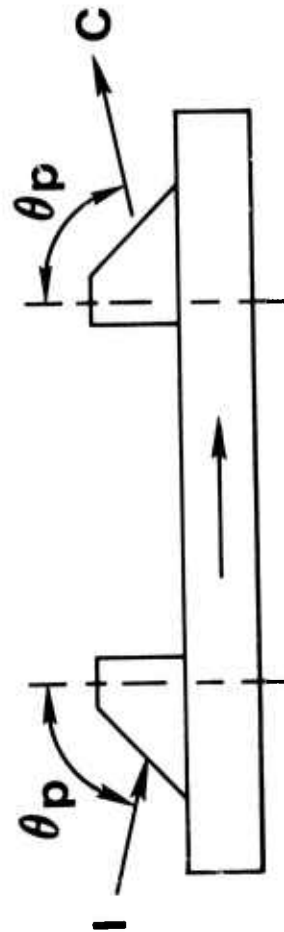
3.5 References

1. Cheo, P. K., D. W. Fradin, and R. Wagner: Microwave Waveguide Modulators for CO_2 Lasers. Fifth Semi-Annual Technical Report, Contract No. N00014-73-C-0087 (March 1975).

2. Cheo, P. K., M. Gilden, and R. Wagner: Microwave Waveguide Modulators for CO_2 Lasers. Sixth Semi-Annual Technical Report, Contract No. N00014-73-C-0037 (Sept. 1975).

3. Fradin, D. W., P. K. Cheo, S. T. Peng, and T. Tamir: Paper WD2 in OSA Topical Conference on Integrated Optics. Salt Lake City, Utah, January 12-14, 1976.

4. Tamir, T.: Inhomogeneous Wave Types at Planar Interfaces III: Leaky Waves. Optik 38, 269 (1973).

5. Yariv, A.: Coupled Mode Theory for Guided-Wave Optics. IEEE, J. Quant. Electr. QE-9, 919 (1973).

6. Tamir, T., and H. L. Bertoni: Lateral Displacements of Optical Beams at Multilayered and Periodic Structures. J. Opt. Soc. Amer. 61, 1397 (1971).

7. Peng, S. T. and T. Tamir: Directional Blazing of Waves Guided by Asymmetric Dielectric Gratings. Opt. Commo. 11, 405 (1974).

EXPERIMENTAL CONFIGURATIONS

(a) Grating coupler

(b) Prism coupler

FIG. 3.1

7601-35-2

UNITED TECHNOLOGIES
RESEARCH CENTER

3-14

FIG. 3.2

INPUT COUPLING EFFICIENCY

$$\eta = \eta_A \eta \,\text{U.B.}$$

$R = 0.65/\alpha$

$D = 1.3/\alpha$

$D = 2R \approx 1/\alpha$

αR

η
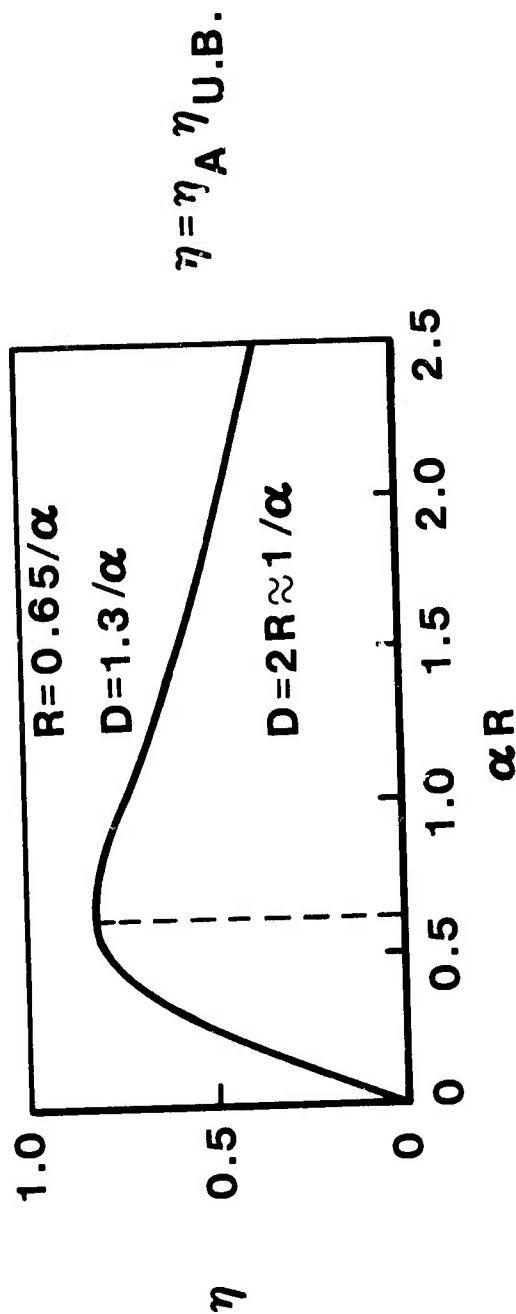
FIG. 3.3

ANGULAR MISMATCH
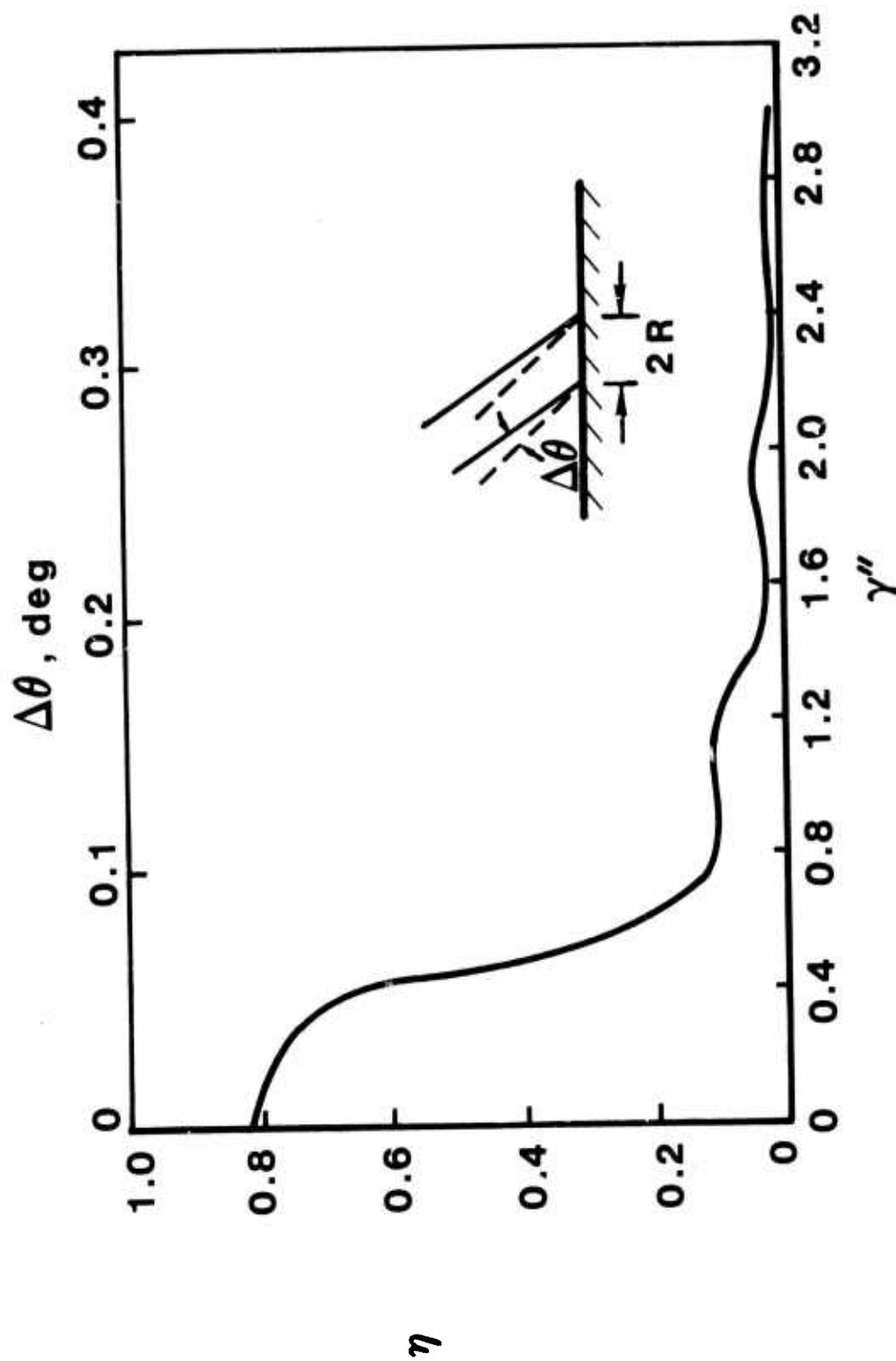
GRATING COUPLING ANGLES AS A FUNCTION OF WAVEGUIDE THICKNESS

$n = 3.275$
$\lambda/\Lambda = 3.855$

FIG. 3.4

FIG. 3.5
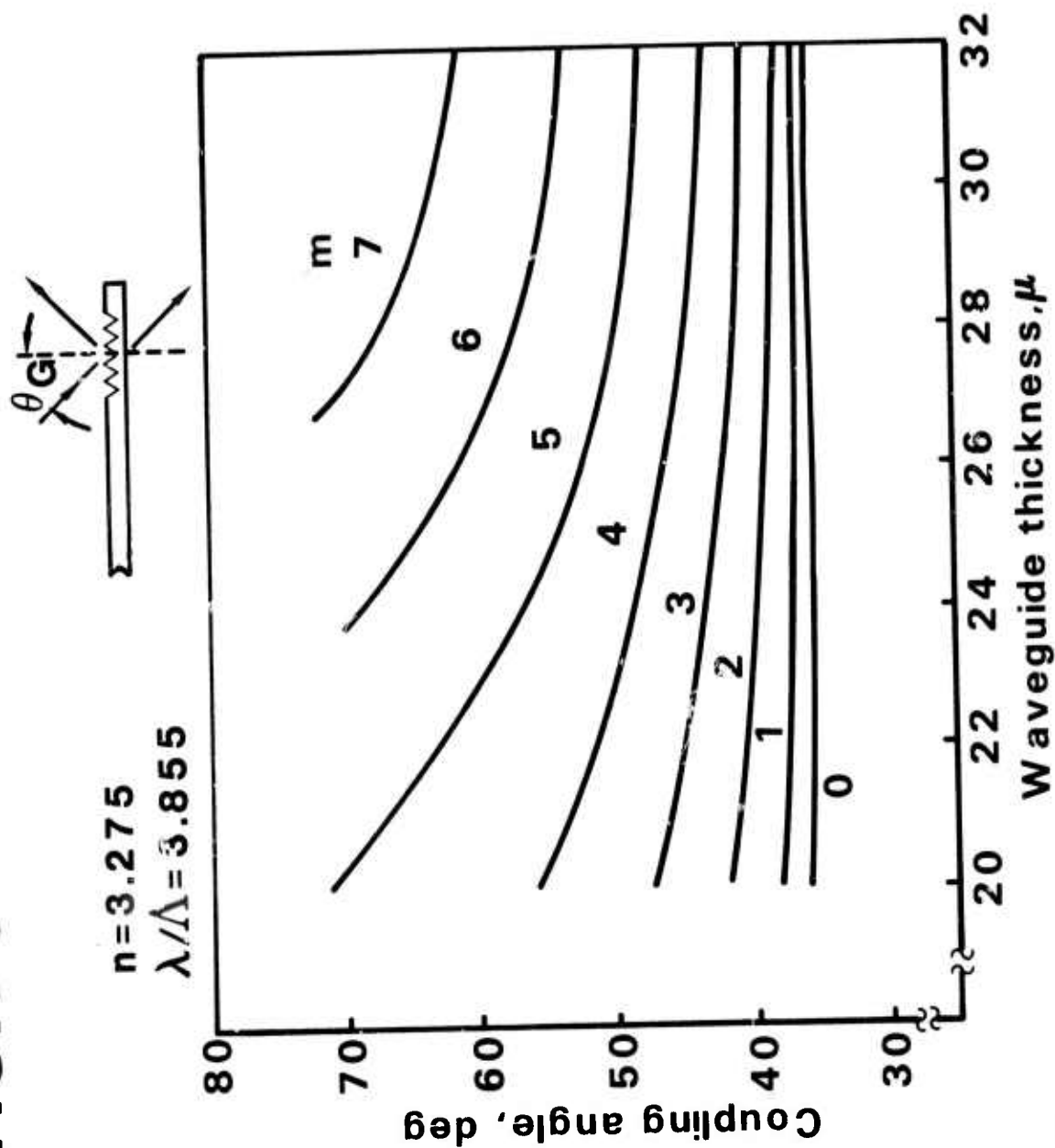
LOSS IN COUPLING EFFICIENCY FROM THICKNESS TAPER

TE$_4$ mode
Beam diameter =1mm
Waveguide thickness=24μ
Groove depth=2μ

Input coupling efficiency, percent

Thickness taper,μ/mm

UNITED TECHNOLOGIES
RESEARCH CENTER
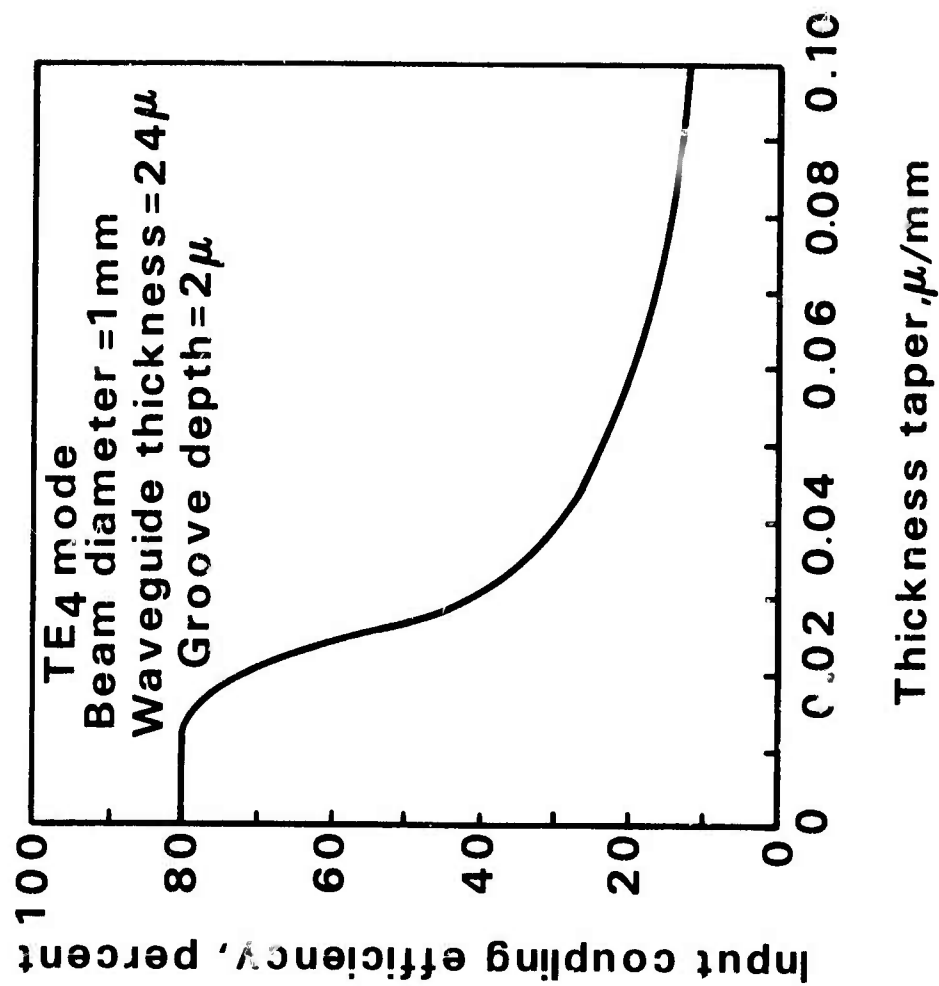
FIG. 3.6

76–03–203–1

PREDICTED COUPLING CONSTANT FOR Ge PRISM COUPLER

(Airgap=0.1μ)
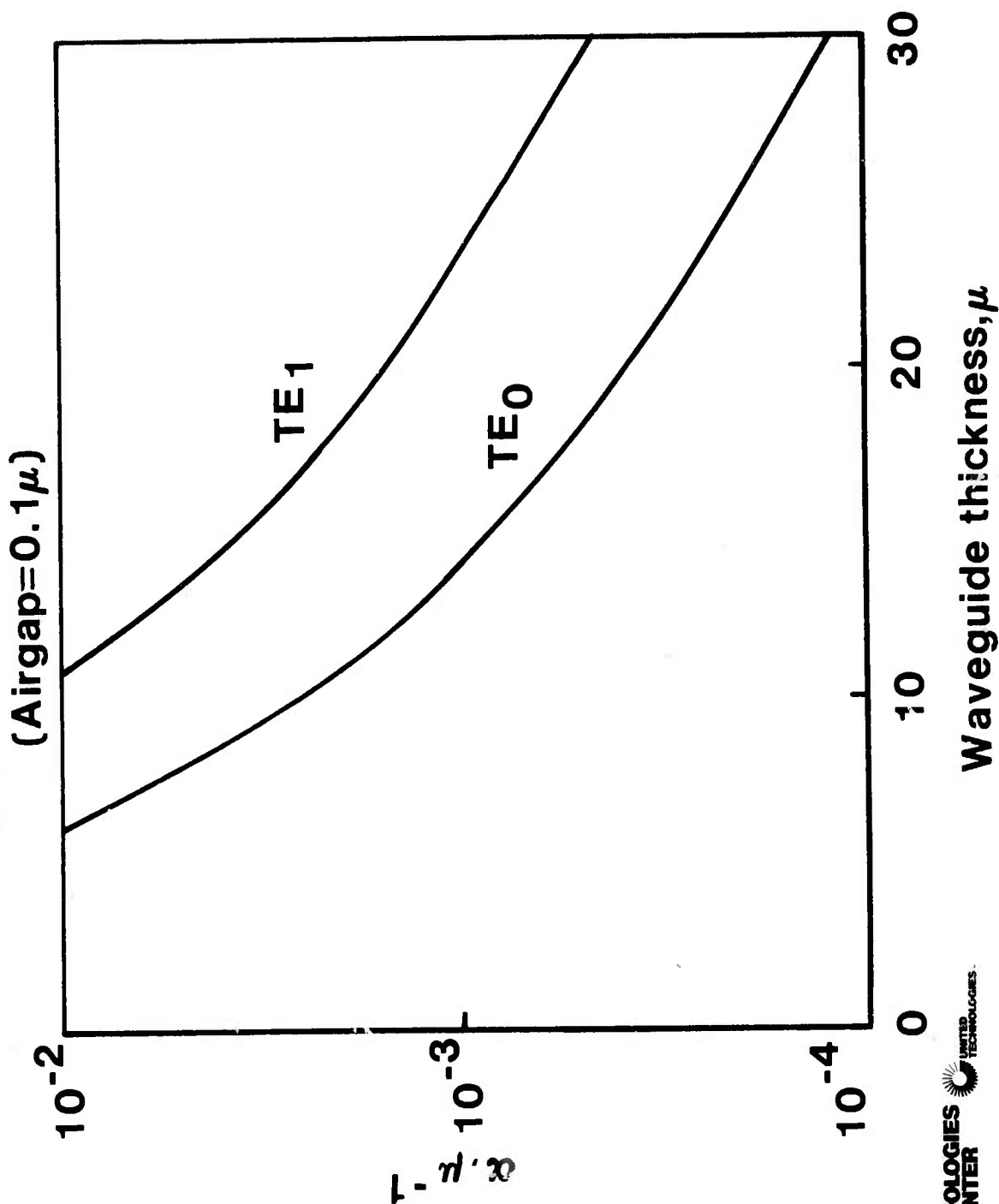
ATTENUATION CONSTANT FOR TE MODES

FIG. 3.7

Groove depth = 2μ

FRACTION OF ENERGY IN UPPER BEAM
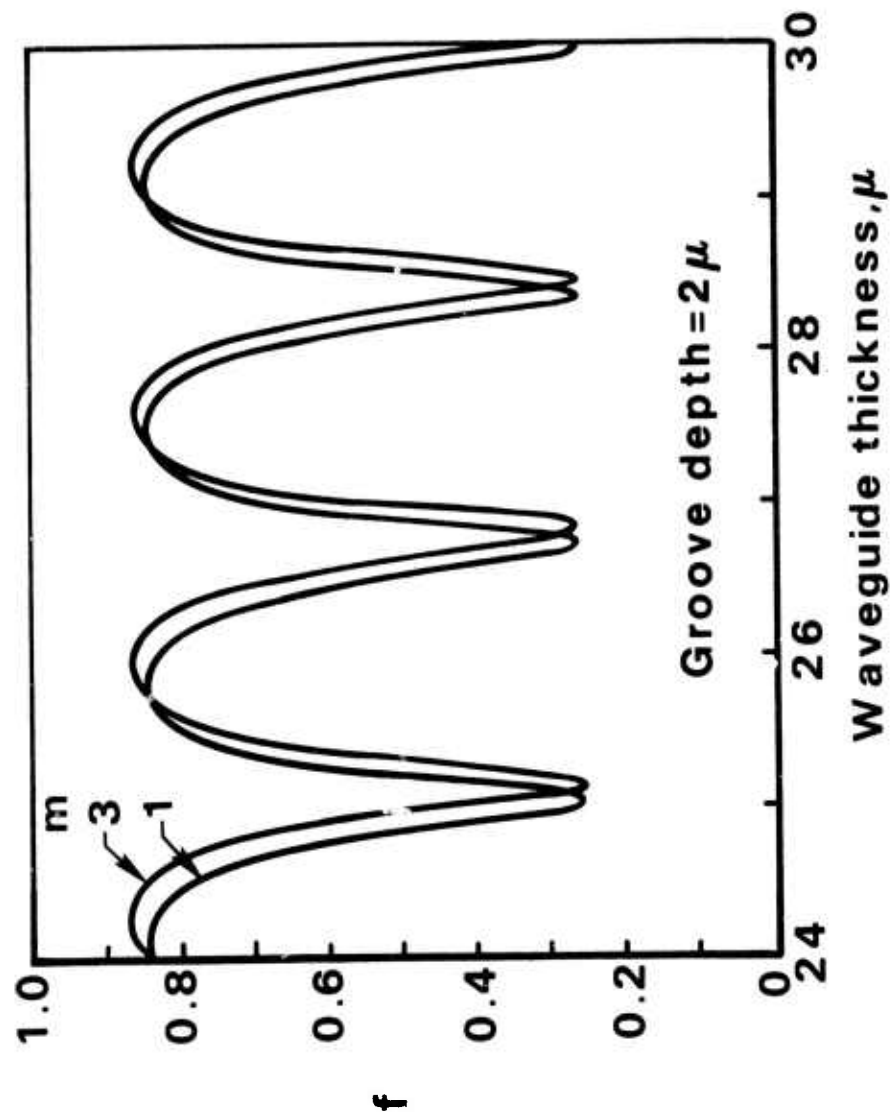
FIG. 3.8

NEAR-FIELD INTENSITY
DISTRIBUTION FOR GRATING COUPLER

FIG. 3.9

76—03—203—2

UNITED TECHNOLOGIES
RESEARCH CENTER

3-22

4.0   WAVEGUIDE FABRICATION TECHNIQUES

4.1   Introduction

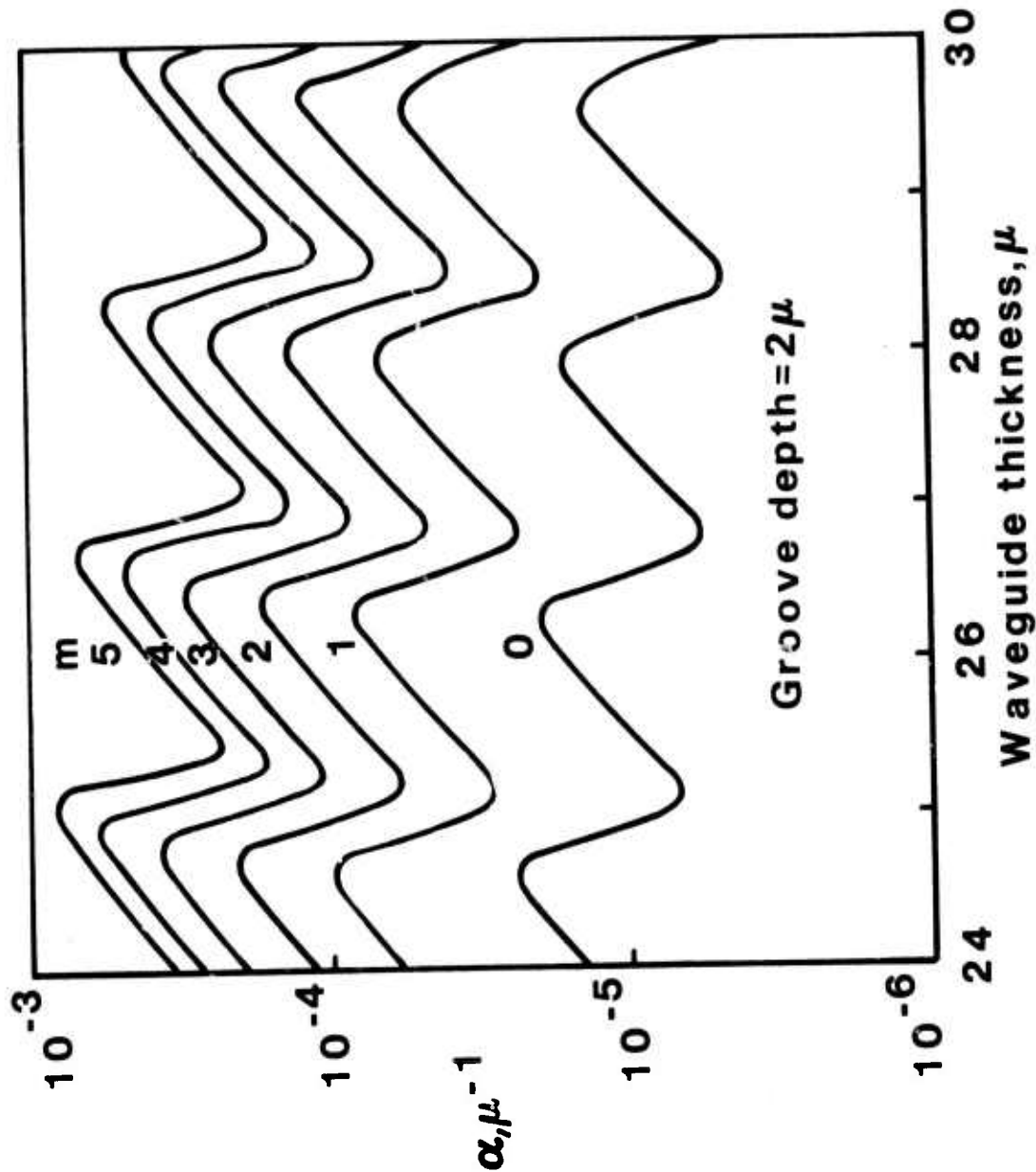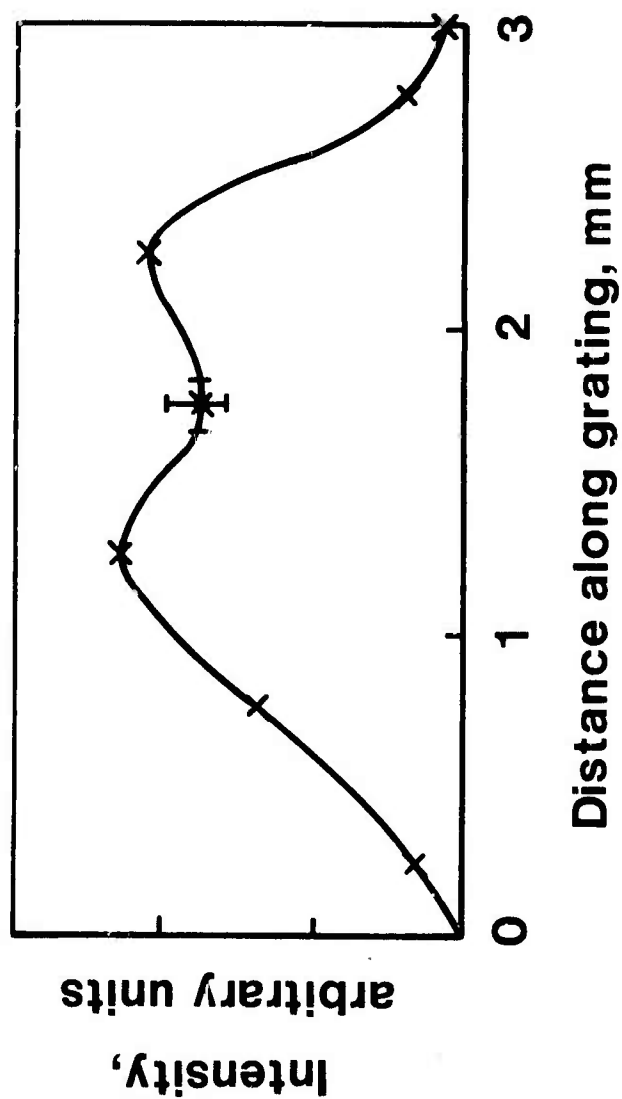Previous studies (Refs. 1,2) indicate that broadband matching of microwave power into a GaAs thin-slab waveguide can be more efficiently and reproducibly achieved if the top and the bottom copper electrodes with a thickness greater than 10 microns were deposited onto the surfaces of the waveguide. To maintain the integrity of the waveguide it is necessary to bond the metal-cladded thin dielectric slab to a flat copper block. Previously we found (Ref. 3) that optical transmission through these waveguides by using prisms as couplers is about ten-times that of grating couplers. A bonded waveguide should provide the structural strength that permits the use of a pair of press-down prisms as the input and the output couplers. Such a structure not only provides the necessary strength and rigidity but also improves the power-handling capability. With proper bonding and heat-sinking techniques, we have demonstrated that these GaAs thin-slab waveguides ($\sim$ 25 μm thick) can handle a combined optical and microwave power which exceeds 100 watts.

Techniques have been developed to produce routinely the bonded GaAs metal-cladded thin-slab waveguides with the specifications listed in Table I. In the following sections, procedures for processing and fabrication of high power infrared waveguides and microstrip transmission lines are detailed.

Table I - Infrared Waveguide Specifications

Thickness	25 μm $\pm$ 1 μm
Length	>4 cm
Surface Finish	Mirror-like
Microstrip Electrode	1 mm x 2.8 cm (10 μm thick)
Bonding Layer	$\lesssim$ 2 um
Copper Block	Optical flat and parallel to 2 sec

4.2 Waveguide Fabrication Processes

Figure 4.1 depicts the infrared waveguide structure. The optical polishing fixture with precision angular adjustments, as shwon in Fig. 4.1, is a very important tool during the initial portion of fabrication process. Carefully selected and electrical characterized high resistivity Cr-doped GaAs ingots in large size are sliced into thin wafers at the orientation (100) plane. The thickness of these saw-cut wafers is typically at 15 mils. The typical wafer size is large enough to yield 3 (1 cm x 4.5 cm) rectangular waveguides. A typical bonded GaAs thin slab waveguide, mounted in a laboratory jig, is shown in Fig. 4.2. The structure is resting on two sliding wedges which are used to control the air-gap for prism couplers, when the top of the two prisms is pressed against a cover plate.

The first step in the fabrication procedure is to lap and polish one face of a .015" thick GaAs wafer. This is accomplished by waxing the wafer to a flat stainless steel block, which in turn is fastened to a polishing jig as shown in Fig. 4.3. This precision polishing jig was developed by Bennet and Wilson, Ref. 4. It consists of an outer holder into which a hardened steel sleeve has been pressed. Also attached to the holder are three steel legs, the ends of which are hardened, and ride on the surface of the lapping plate. A piston runs inside the steel sleeve with a lapped sliding fit. Angular adjustments are provided for fine corrections of the orientation of the copper block and GaAs wafer with respect to the lapping surface at various stages of the lapping process.

Parallelism between wafer surfaces is the most crucial and difficult parameter to control during the fabrication process. A relatively inexpensive but very reliable system, as shown in Fig. 4.4, has been devised to provide accurate measurement of thickness variation over a large surface area without physical contact of the sample. The main part of this system is a noncontacting air gauge head, a Hoverprobe manufactured by Ames-Mercer and an electronic readout with a 3 μm full scale in 0.05 μm divisions. The Hoverprobe is mounted on a steel shaft which is attached to an X-Y table with provisions for angular tilt adjustment. The optical polishing jig to which is fastened either the waxed down GaAs wafer on a flat steel block, or the bonded waveguide to a flat copper block, which is then placed on this X-Y table, as shown in Fig. 4.4.

The surface of either the flat steel block or the flat copper block can then be aligned in parallel with the three hardened steel legs on the polishing jig with the help of the Hoverprobe. Initially, the Hoverprobe is referenced to a zero center scale reading on one of the hardened steel legs. Subsequently, the two other hardened steel legs are brought under the Hoverprobe. By adjusting the appropriate micrometer head on the tilt table these legs can be adjusted to yield the zero reference. In this way all three legs are made parallel to the Hoverprobe. The Hoverprobe is then placed above the surface of either the flat steel or flat copper block. By the same technique, one can adjust the block surface parallel to the hardened steel legs.

   With these preliminary alignment procedures, the initial lapping of GaAs sample
is performed by removing about 5 mils thick of material. This is done by using 3 μm
platelet alumina on a glass plate which is fitted to an eccentric type lapping and
polishing machine, manufactured by GeoScience Corp. The GaAs wafer is polished by
using a Politex Supreme pad, saturated with a solution of 100 ml distilled water to
6 ml of 6% sodium hypochlorite. A mirror-like finish is obtained when approximately
10 μm of GaAs is removed.

   The wafer is further thinned by using ion beam milling machining (A Vecco Micro-
tech System) and coated with a thin layer of a copper film. Prior to ion beam machin-
ing, the wafer is removed from the steel block and cleaved into 4.5 cm x 1.0 cm wave-
guide strips. These strips are attached to a copper block with Apeizon type vacuum
grease with the polished side up. The copper block containing the waveguide section
is mounted on a rotating substrate holder oriented at an angle normal to a collimated
beam of Ar^+ ions. The polished surface of the GaAs is ion milled at a current density
of 1.0 mA/cm^2. The rate of removal is 8 μm/hour. Ion milling proceeds until 25 μm
of material is removed. A thin layer of 1 μm copper film is subsequently deposited
onto the surface of the GaAs wafer by reorienting the substrate holder in a position
which is in a direct view of a water-cooled copper target.

   This copper coated wafer is removed from the Microetch system and electroplated
in a Sel Rex electroplating both (Cubath I) at a current density of 30 mA/cm^2, until
a copper film with a thickness of 10 μm is obtained. This forms the ground plane of
the waveguide modulator, which is bonded to an optically polished copper block with
Stycast 1217 resin, manufactured by Emerson & Cuming Inc. This low viscosity resin
allows formation of a thin bonding layer of the order of 2 μm thick. Both the thick-
ness and thickness uniformity depend critically on a counterweight system. It consists
of an optically polished steel base, to which a piston ring is attached. A carefully
machined cylindrical weight is free to slide in this ring. On the bottom of the
weight an optically polished rectangular steel pad 4.25 cm long x 0.8 cm wide, is
attached. With only a few drops of properly prepared Stycast 1217 resin applied
to the ground plane, a strong and uniform bonding layer will form at a curing tem-
perature of 160°F by keeping the wafer under the weighted rectangular pad over a
period of one hour.

   The bonded wafer is again mounted in the polishing jig with the alignment pro-
cedure of the copper block face with respect to the 3 steel legs as previously
described. At this point the thickness of the GaAs wafer is about 8 mils. The
waveguide is then lapped until approximately 2 mils of GaAs is removed. The sur-
face is then chemo-mechanically polished to a mirror-like finish. During the
processing, the thickness of the GaAs waveguide is measured at several points
along the 4.5 cm length with a Perkin-Elmer Model 621 IR Spectrophotometer in the
reflectance mode. The thickness variations determined by the IR spectrophotometer
gives an indication of the wedging in the GaAs wafer only. With above described
thinned process wedging is routinely found to be less than 2 μm along the 4.5 cm

length of the .0055" thick waveguide. The IR spectrophotometric measurements can also be compared with the Hoverprobe measurements. In general, very good agreement exists between these two independent measurements, which implies that the copper ground plane and bonding medium are essentially wedgefree. If any wedging does exist at this point it can be compensated by using the angular adjustments which are incorporated in the polishing fixture. The wafer is then lapped to a 2.4 mils thickness, at which a chemo-mechanical polish is performed. Spectrophotometer scans are taken again of the GaAs thickness prior to the final ion beam thinning.

The final ion-beam thinning processing is then carried out. In this process special precaution must be taken to maintain the substrate at a low temperature $< 50°C$. It has been found that the difference in thermal expansion between GaAs and the copper ground plane can cause cleavage in GaAs wafers if the temperature of the substrate is not controlled. A water cooling fixture was installed into the Vecco Microetch System. It was designed specially for the rotating holder to maintain a low temperature ($< 50°C$) under ion-bombardment over extended periods of time. For the final thinning process of bonded waveguides, a current density of .8 mA/cm^2 is used with the rotating fixture oriented at an angle of $45°$ with respect to the ion beam. Under these conditions the removal rate is 8 μm/hr. Ion beam thinning is terminated when the GaAs reaches a thickness of 25 μm. This completes the basic fabrication process of the bonded-down infrared waveguides.

4.3 Microstrip Electrode Fabrication Processes.

To make a microwave modulator a microstrip electrode must be applied to the top surface. Figure 4.5 illustrates the steps taken to form a microstrip electrode on the surface of the bonded thin-slab GaAs waveguide. The waveguide is first spin-coated with Shipley AX1350B as shown in Fig. 4.5a. The photoresist is then exposed and developed, and a 1 μm of copper film is subsequently ion-plated onto the GaAs wafer surface in steps as shown in Fig. 4.5b and c. An overcoat of resist is then applied over the thin copper film and the stripline image exposed and developed out of the resist in steps as shown in Fig. 4.5d and e. The stripline image is then electroplated to a thickness of 11 μm in the copper electroplating bath (Fig. 4.5f). After removing the resist, the thin copper film (1 μm) is etched away in ferric chloride solution. The fabrication of a microwave waveguide modulator is completed after removing the last coat of resist, as shown in Fig. 4.5g.

A two dimensional channel waveguide can be produced by ion milling a bonded GaAs waveguide modulator around the edges of the microstrip electrode. To form the channel, the waveguide is first photoresisted (spin-coated), and then a pattern is exposed and developed as shown in Fig. 4.6a. The photoresist pattern is then ion-plated with 6000 Å of titanium. The titanium plated photoresist is then lifted off in the acetone to yield the pattern as shown in Fig.4.6b. A 4 μm deep channeling is formed by ion milling of the waveguide at a current density of .8 mA/cm^2 for 30 min

at an orientation normal to the ion beam. Titanium was chosen as a milling mask due to its high differential etch rate with respect to GaAs (10 to 1). An added advantage of a titanium etch mask is that any remaining titanium can be etched with HF without degrading the GaAs surface.

4.4 References

1.   Cheo, P. K. and M. Gilden: Appl. Phys. Lett., 25 272 (1974).

2.   Cheo, P. K., M. Gilden and R. Wagner: Infrared Waveguide Modulators at Micro-wave Frequencies, 6th Semi-Annual Tech. Rept., Contr. No. N00014-73-C-0087, Sept. 1975.

3.   Cheo, P. K., D. W. Fradin and R. Wagner: Microwave Waveguide Modulator for CO_2 Lasers, 5th Semi-Annual Tech. Rept., Contr. No. N00014-73-C-0087, March 1975.

4.   Bennett, G. A. and R. B. Wilson, J. Sci. Inst., 43 669 (1966).

TYPICAL HIGH-POWER IR WAVEGUIDE STRUCTURE

Cu stripline

Ge prism

GaAs thin-slab waveguide

Cu ground plane (10 μm thick)

Low viscosity Epoxy bond (≈ 2 μm)

Optically polished Cu block (1/4 in.)

Optical polishing fixture

3 adjustments at 120° spacing

FIG. 4.1
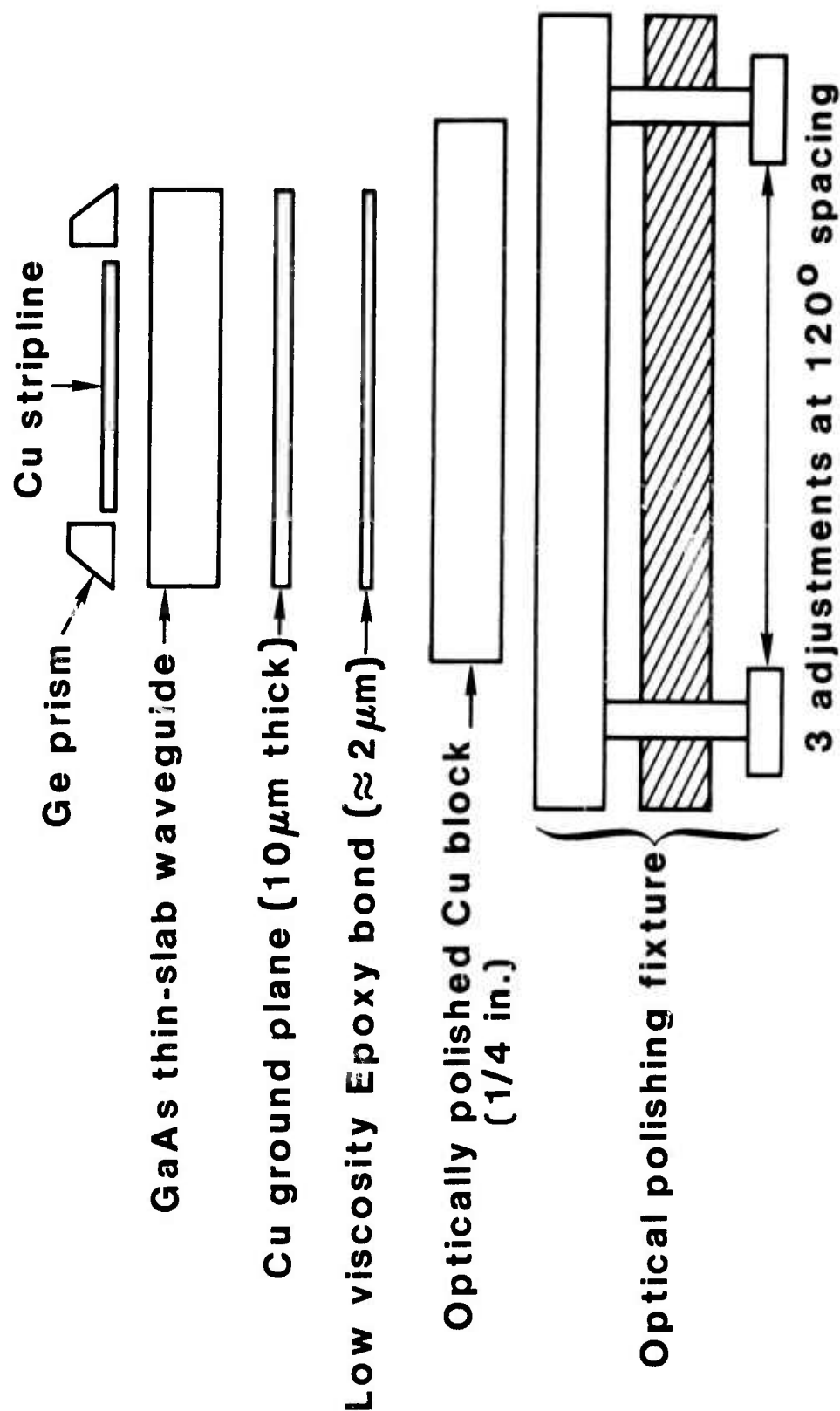
FIG 4.2

RO9-176-3

INFRARED WAVEGUIDE
HOLDER ASSEMBLY

Ge Prism

GaAs Waveguide

Cu Block

Waveguide
Modulator Holder

1 INCH
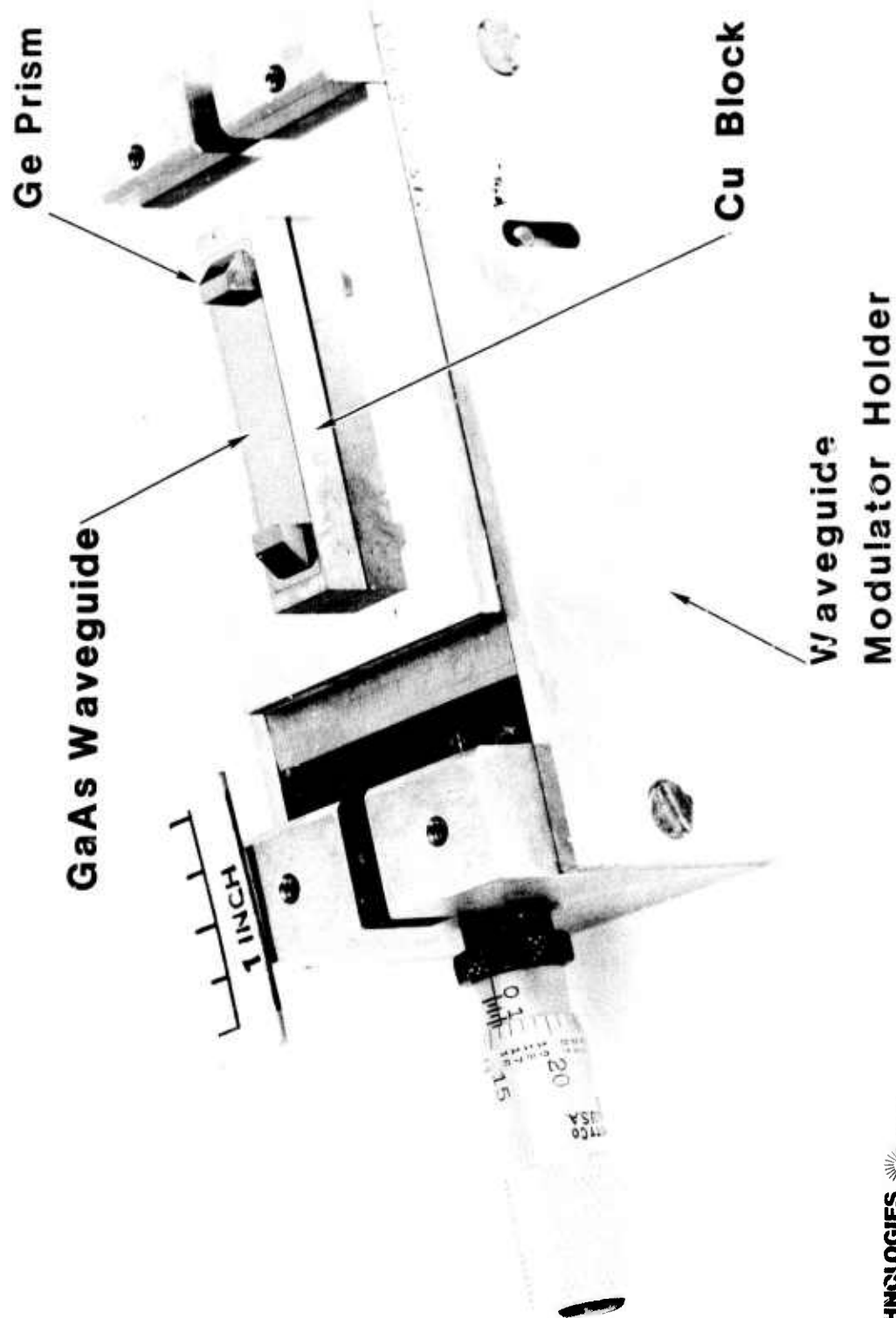
FIG. 4.3

PRECISION POLISHING JIG FOR
GaAs WAVEGUIDES

1 INCH

RO9—178—3

UNITED TECHNOLOGIES
RESEARCH CENTER
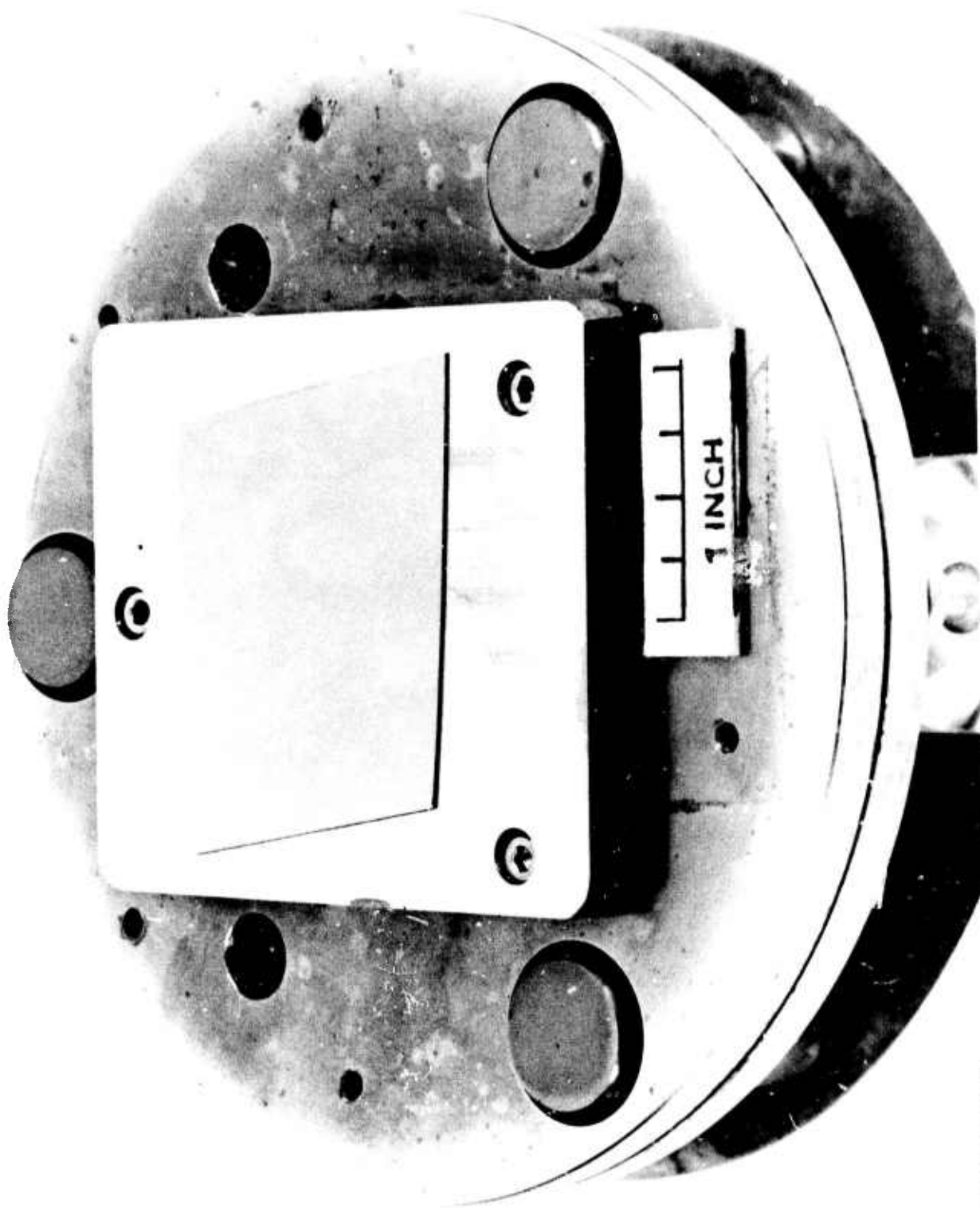
FIG. 4.4

X - Y TABLE WITH HOVER PROBE

Noncontacting gauge head.

Hardened steel legs

GaAs waveguide

Cu block

Angular adjustment

Tilt table

FIG. 4.5

76-02-237-2

UPPER ELECTRODE FABRICATION

(a) Photoresist

AZ1350B

(b) Expose/develop resist

AZ 1350B | AZ 1350B

(c) Ion plate, $1\,\mu m$ Cu

$1\,\mu m$ Cu

(d) Photoresist ion-plated Cu

AZ1350B Overcoat

(e) Expose/develop microstrip pattern

AZ 1350B | AZ 1350

(f) Electroplate to $11\,\mu m$ Cu

AZ 1350B | AZ 1350B

(g) Strip resist/etch back $1\,\mu m$ Cu/strip resist
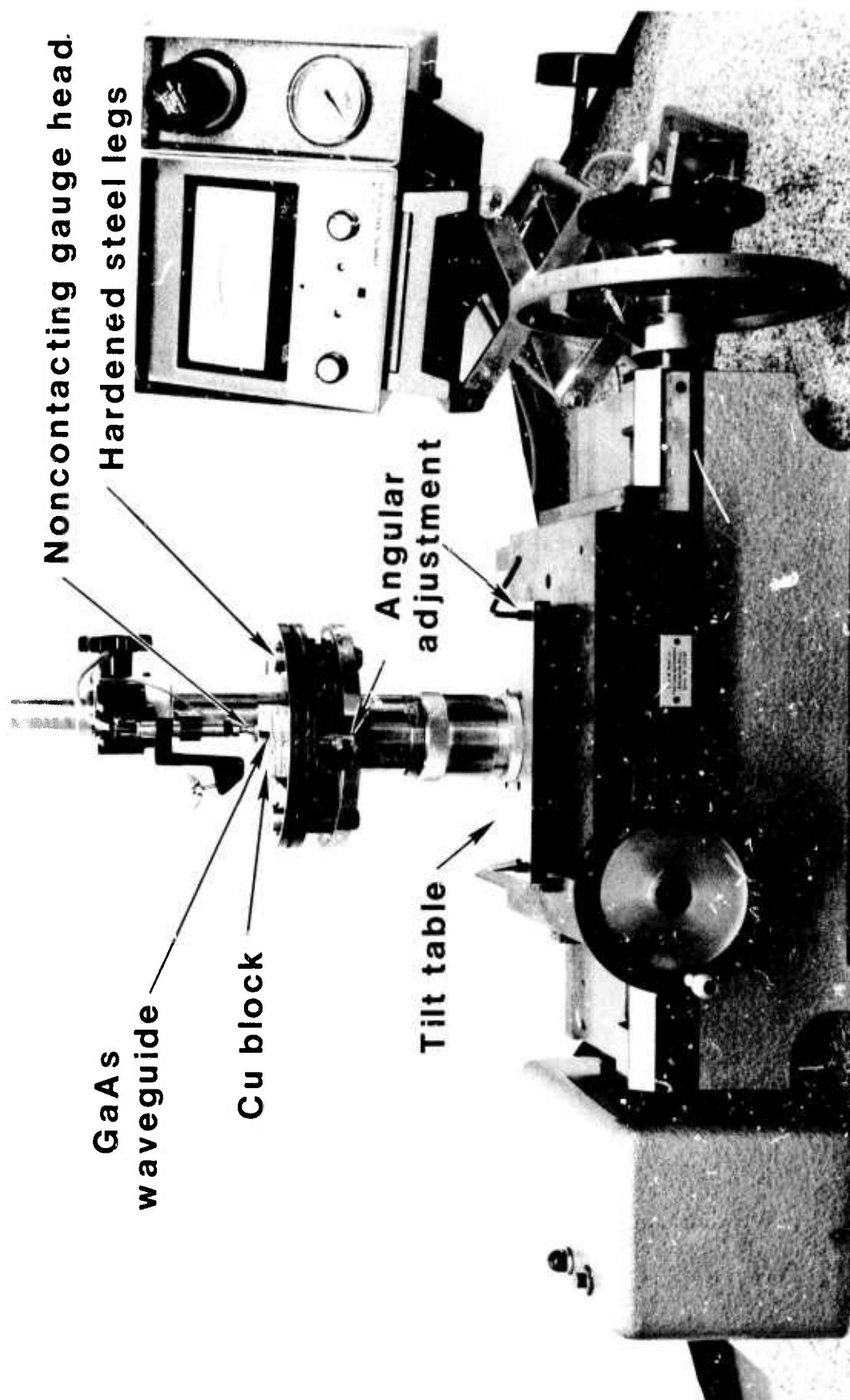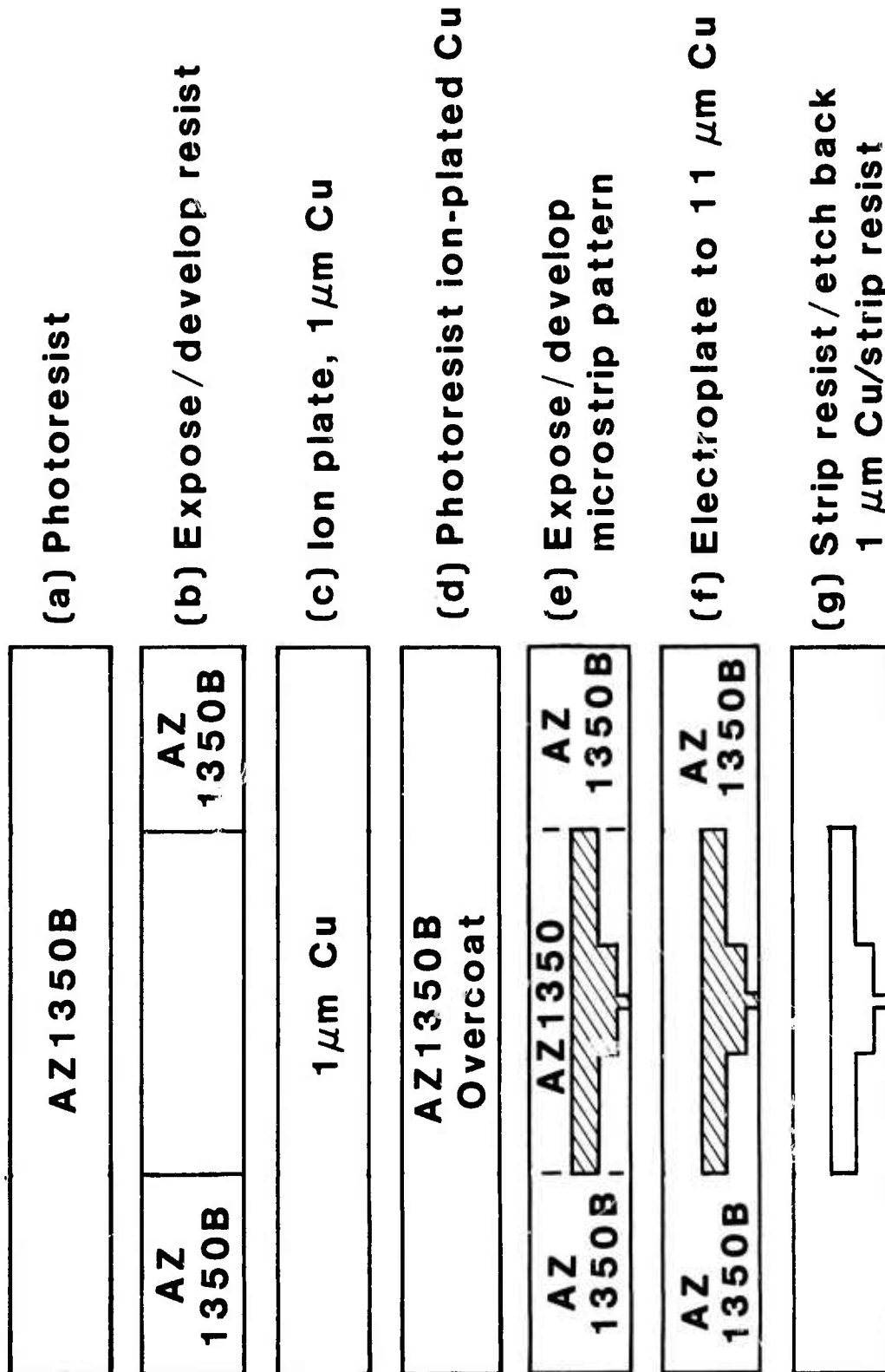
FIG. 4.6

CHANNEL WAVEGUIDE FABRICATION

a)

AZ1350

AZ1350   AZ1350

b)

GaAs

GaAs   GaAs

$6000 \overset{\circ}{A}$

T_i

5.0 BROADBAND MICROWAVE MODULATOR CIRCUITS

5.1 Introduction

Broadband modulator characteristics requires the application of microwave impedance matching techniques to the microstrip transmission lines formed by the modulator electrodes and the input lines. Since these lines are unconventional in size compared to those commonly used for microwave components, it was necessary to determine experimentally the circuit parameters of the microstrip lines as was done earlier for the mini-gap ridge waveguide (Refs. 1, 2). Measurements were made of the characteristic impedance, the effective dielectric constant and the attenuation coefficient.
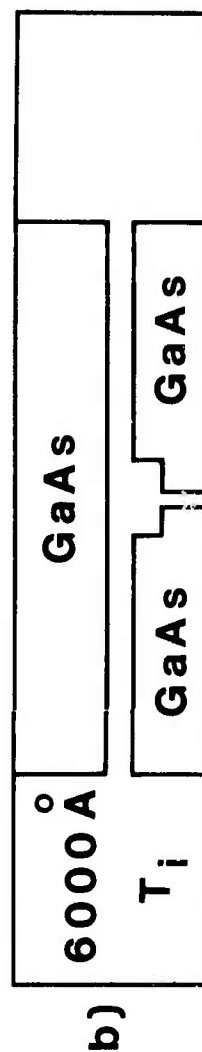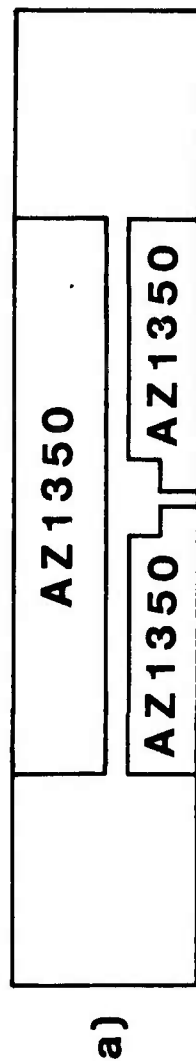
In anticipation of high power microwave operation up to 100 watt levels, it was felt that the input circuits to the microstrip modulator should be made of a tapered ridge waveguide, since the solid material ridge provides a good low thermal resistance path to a heat sink. However, both the ridge waveguide and the small compact coaxial input connectors (SMA) were evaluated at power levels up to 80 watts while connected to the GaAs waveguide modulator. The results indicated that the small coaxial input line is capable of handling 80 watt power and it has been used in subsequent experiments. For continuous operation over a long time period and/or at a higher power level, a ridge waveguide would be the best choice.

The microwave microstrip circuit is shown in more detail in Fig. 5.1. The electrode is center-fed through a microstrip impedance transformer from a coaxial microstrip launcher and the ends are open circuited. The launcher, a standard design, was modified to have a longer center conductor extension and semicircular shield. The longer extension allowed the pressure to be distributed over a wider area on the GaAs thin-slab without causing material damage. The larger contact area for the microwaves also provided slight adjustments for improving the input impedance matching. With the center fed excitation of the microstrip transmission line, only the wave that is in synchronous with the laser beam modulates this guided optical wave (Refs. 2, 3). At the center frequency the electrical distances are integral numbers of half wavelengths from the feedpoint to the open circuited ends. Although the configuration may seem narrow band, this is not necessarily the case as will be shown by detailed computer modeling of the microwave circuit in the next section. For example, if the feed line from a matched generator is well matched to the net characteristic impedance of the two lines in parallel, then the amplitudes of the synchronous components of the standing wave are independent of frequency. Therefore, a broad band operation can be accomplished by placing a microwave circulator at the input port that not only protects the modulator driver by providing a matched termination for the reflected power but also produces a circuit that is almost equivalent to that of a two port modulator.

The most efficient modulation condition, of course, occurs when the net input resistance is transformed so that an impedance match exists at the input port of the modulator. Under these matched conditions an expression for the power in the sidebands has been derived (Refs. 2, 3) and repeated here for reference

$$P_{SB} = \left(\frac{\Delta\phi}{2}\right) P_0 \qquad (5-1)$$

in which the phase shift $\Delta\phi$ is

$$\Delta\phi = \frac{k}{4} r_{41} n^3 \left(\frac{2P \eta L}{tw\alpha}\right)^{1/2} \qquad (5-2)$$

where $r_{41} = 1.2 \times 10^{-10}$ cm/volt, n is the index of refraction, $k = 2\pi/\lambda$, P is the microwave power, α is the microwave attenuation coefficient in Nepers, η is the free space characteristic impedance, t is the slab thickness and W is the width of the microstrip line, and L is the length.

5.2 Modulator Circuit Modeling

A better understanding of the possible range of modulator bandwidths was obtained from a computer circuit model by varying parameters corresponding to the microstrip modulator circuit. The transmission line characteristics used in the analysis were determined experimentally from measurements on long straight sections. The resonant frequencies and the input impedances at resonance, were used to establish the following values for a modulator microstrip line whose physical dimensions are 25 microns thick and 1 mm wide: Characteristic impedance (Z_0) = 2.7 ohms, attenuation = 0.70 dB/cm and an effective index of refraction = 3.5.

The microwave circuit analyzed consisted of the elements shown in Fig. 5.2. The modulator line is of length L, of characteristic impedance Z_0 and is open circuited at both ends. In the analysis the input line and impedance transformers forming the center feed, in Fig. 5.2, may have all or some of the elements shown and will be so indicated in the various examples discussed below. The short lengths of line of characteristic impedance Z_1 and Z_2 are taken to be quarter wavelength at the center frequency and the generator impedance, R_{gen}, will typically be 50 ohms, but other values will also be used. The incident and reflected power at the generator terminals are denoted by P_I and P_R respectively while at the actual junction to the modulator line, the incident and reflected power are denoted as P_i and P_r respectively. In Fig. 5.2 a synchronous component of microwave, P_{sync}, is identified at the output end of the modulator. In the calculations an approximate average value of this component across the length of the line will be used in order to account for wave attenuation. This average value of P_{sync} is proportional to the side band power generated by the modulator.

Before proceeding to the bandwidth analysis, the relative power in the synchronous wave at the input terminals to one half of the modulator has been calculated as a function of the attenuation of the line and the ratio of Z_1 to Z_0. The results are shown in Fig. 5.3. In this case the line is assumed to be an integral number of half wavelengths long and open circuited at the end. Since only one section of the modulation is being treated, Z_1 corresponds to twice the value that would be used for the full modulator and P_I is only one half the incident power. It is also assumed that $Z_1 = R_{gen}$ with reference to the definitions in Fig. 5.2 and 5.3. By definition, when the modulator characteristic impedance is equal to that of the input line the synchronous power equals the incident power and the traveling wave condition pertains. The curves plotted in Fig. 5.3 show that the smaller is the attenuation in the line, the larger is the maximum possible value of the synchronous power. At a given level of attenuation, the maximum value of the synchronous wave actually corresponds to the input line, Z_1, being matched to the net resistance appearing at the input terminals, R_{in}. The levels of attenuation from 1 to 3 dB are typical values for the microstrip modulator lines actually tested. Attaining the largest possible synchronous wave amplitude, however, is not compatible with the largest bandwidth.

The frequency response of the actual modulator is first analyzed by assuming the idealized condition that the input line consists of only a driving generator whose impedance, R_{gen}, is frequency independent (See Fig. 5.2). These calculations involve the well known general transmission line equations, in which the necessary inclusion of wave attenuation requires that hyperbolic functions with complex arguments be evaluated. Where more than two sets of terminals are present, the use of a computer program dedicated to microwave circuit analysis greatly expedites calculations (Ref. 4). Figures 5.4 and 5.5 present the calculated results for two idealized cases: (1) a value of generator impedance of 2.5 ohms (approximately equal to the characteristic impedance of the modulator), and (2) a value of 10 ohms (approximately equal to the net input resistance of a 12 wavelength long modulator). These calculated results provide a quantitative picture of how the frequency response, in terms of P_{sync}, depends upon modulator length, L, when wave attenuation is taken into account. The frequency response is found to be widest for the shortest length, however, with shorter lengths conversion efficiency is reduced (Refs. 2, 3). For completeness the variation of modulator input resistance is also shown in Fig. 5.4 as function of frequency. Its variation is seen to be not indicative of the modulator response. For the 12λ modulator (most of the modulation experiments have been made with this length), it is interesting to note that a much wider bandwidth i.e., 700 MHz, can be obtained from the 2.5 ohms generator, as compared to 200 MHz for the 10 ohms generator. The additional bandwidth can be gained with a trade-off in reduction of synchronous power by only 2 dB. The synchronous component of power, as mentioned earlier, was evaluated at the exit end of the modulator and represents an approximate average value over the length of the modulator. The calculations were not carried to values below 2.5 ohms because at present it does not seem practical to consider fabricating impedance

transformers for such low values. The circuit losses at such low values can be
detrimental. These calculations establish that the open-ended waveguide modulators
with a bandwidth exceeding 1000 MHz are possible. This structure has been
referred to as a "resonant structure" in our preceding work (Ref. 3).

In this computer modeling of the microwave circuit, for simplicity, no
provisions were made to compute the effective phase shift modulation by taking
into account the exact field distribution of the synchronous wave. Nevertheless
the value of the component of synchronous power at the exit end of the modulator
represents a useful mean value for comparison purposes. As an example, compare
the 12λ center-fed modulator of Fig. 5.4 to a 12λ modulator with only a traveling
wave. The traveling wave would be excited from a matched generator at one end and
the microwave power delivered to a matched level at the other end. Since the
attenuation for 12λ long modulator is approximately 2 dB, a mean value of -1 dB
might be used for the traveling wave case. The zero dB levels in Figs. 5.4 and 5.5
correspond to the modulation characteristics that would be obtained with a traveling
wave where no microwave attenuation existed. Comparing this with the center-fed
modulator with the open circuited ends, we see that the center-fed modulator has
a value for P_{sync} of -2 dB. This is only one dB less effective than the traveling
wave structure.

We next consider what bandwidths would be obtained with the microstrip circuit
if impedance transformers were formed in the input microstrip line in order to
obtain desirable values of equivalent generator impedances. The impedance trans-
formers would consist of $\lambda/4$ lengths of microstrip lines with selected impedance
values, as was illustrated in Fig. 5.2. The values of impedance for a particular
transformer ratio and the type of frequency response, depending upon maximum standing
wave ratio in the pass band, can be obtained from published theoretical results
(Ref. 5). In view of the bandwidths already demonstrated in Figs. 5.4 and 5.5,
impedance transformers with 30 percent bandwidth were selected. These can be
realized with the existing circuits without further advancing fabrication techniques.
The results of calculations on the 12λ structure are given in Fig. 5.6 for various
transformer ratios and a 50 ohm source. Results are indicated for a one-step and
several two-step transformers. A bandwidth of 600 MHz is obtained for the 50 ohm
generator impedance transformed down to 2.5 ohms. This compares favorably with
the 700 MHz obtained from Fig. 5.4 where a constant resistance generator impedance
of 2.5 ohms was assumed. It is also interesting to note, for the 4.2:1 transformer
value, that both a one step and a broader band two step transformer gave essentially
identical modulator bandwidths. This indicates that both impedance transformers
were sufficiently wide and that the limiting factor was primarily the main modulator
line itself. Further bandwidth improvement using a single input port would require
a new approach.

5.3 Experimental Results on Bandwidth

The theoretical calculations on bandwidth predict reasonably well the experimentally measured bandwidths that are obtained by measuring the actual optical side band power variation as a function of frequency. An experimental result for a 12λ modulator, center-fed through a two step transformer is given in Fig. 5.7. The bandwidth obtained is 700 MHz and the conversion efficient is 0.7 percent. In these measurements the sideband power was obtained using the scanning Fabry-Perot interferometer as discussed in previous reports. This data was taken after the various improvements on the modulator detailed earlier in this report were realized. The measured data points were corrected for small drifts in microwave power and optical power and are seen to represent relatively little scatter. This experimental data actually has better bandwidth than the theoretical model predicts. With these results and the results (Fig. 6.4) showing 1 GHz of bandwidth, it is evident that a center-fed modulator through a two step transformer would be sufficient to meet the requirement of this program. It is possible to make the present structure even broader band and to obtain a better control on the detailed shape of the frequency response of the side band power with our modeling techniques.

5.4 References

1. Cheo, P. K., M. Gilden, J. F. Black and J. S. Swindal: UARL Semi-Annual Tech. Report M921513-4, September 1973, Contract No. N00014-73-C-0087.

2. Cheo, P. K., and M. Gilden, Appl. Phys. Lett. $\underline{25}$, 272 (1974).

3. Cheo, P. K., M. Gilden, D. Fradin and R. Wagner: UARL Semi-Annual Tech. Report N921513-6, March 1974, Contract No. N00014-23-C-0087.

4. Computer Program "MAP" Developed by ECI Software Corp.

5. Young, L., E.R.E. Trans. $\underline{MTT-7}$ 233, (1959).

IR MODULATOR-MICROSTRIP MICROWAVE SECTION

Connector

Coax - microstrip transition

Microstrip (electrode)

Optical path

GaAs

Metallic base

FIG. 5.1

76—03—63—6

UNITED TECHNOLOGIES RESEARCH CENTER
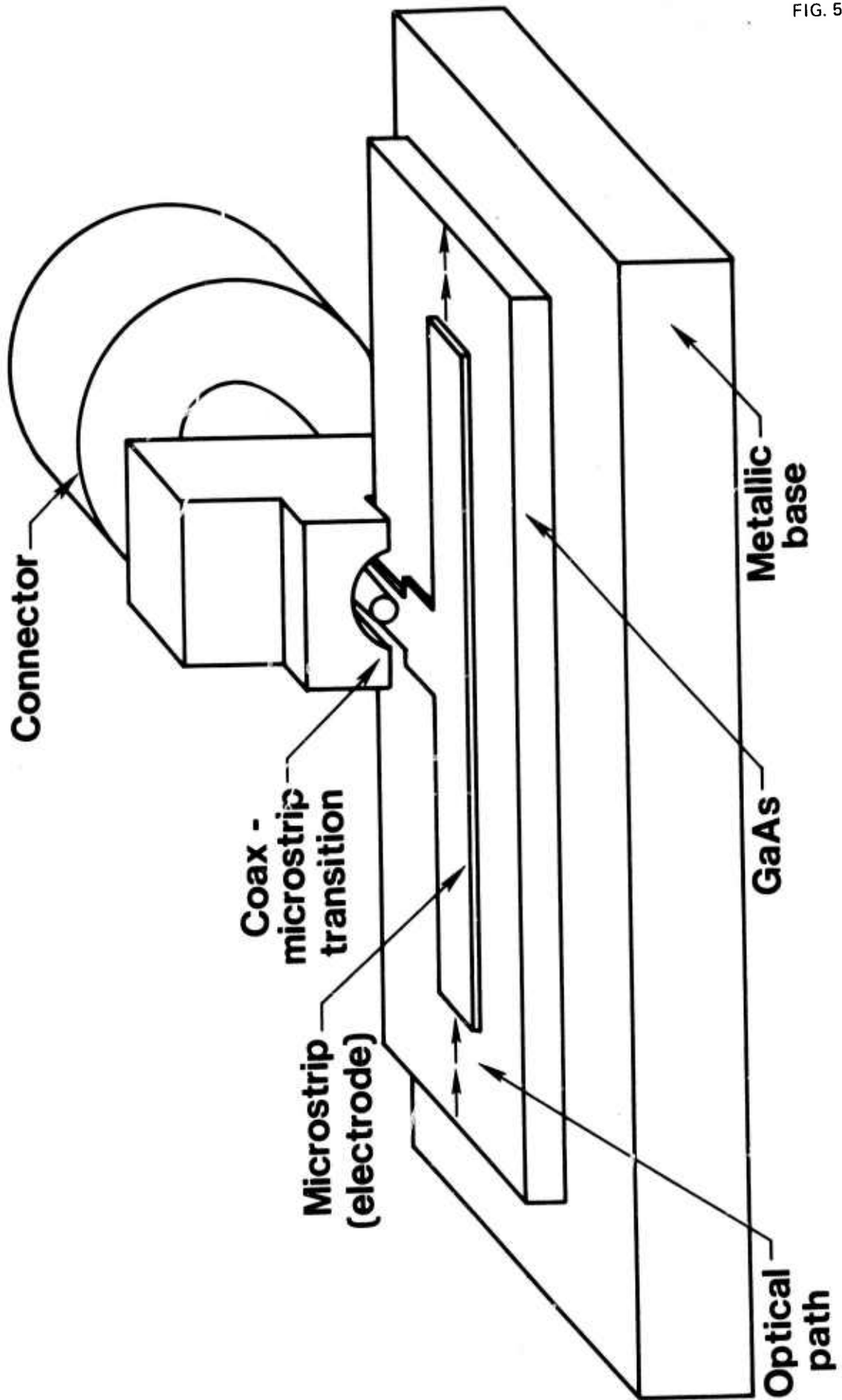
MODULATOR CIRCUIT MODEL
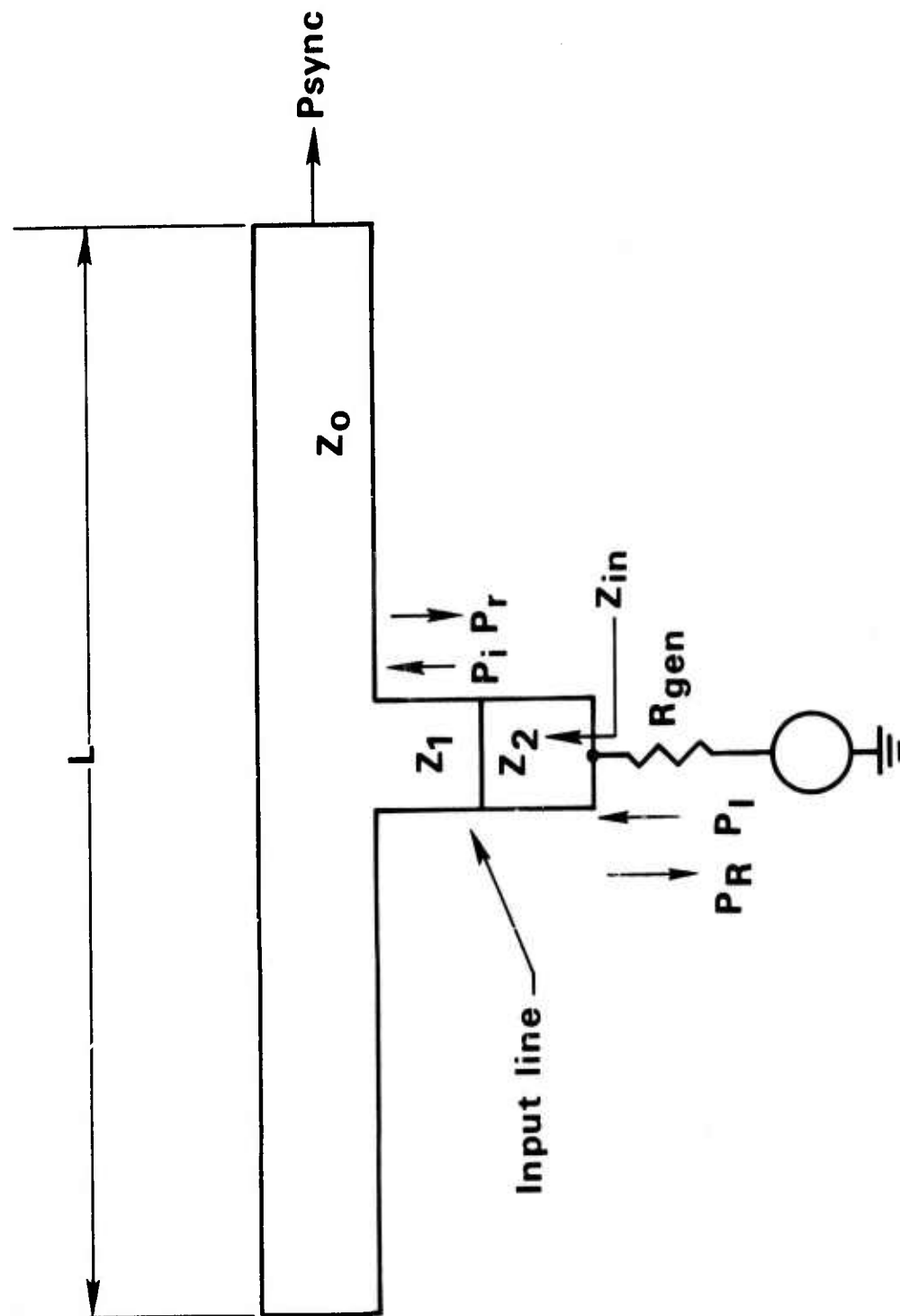
FIG. 5.2

RELATIVE POWER IN SYNCHRONOUS WAVE
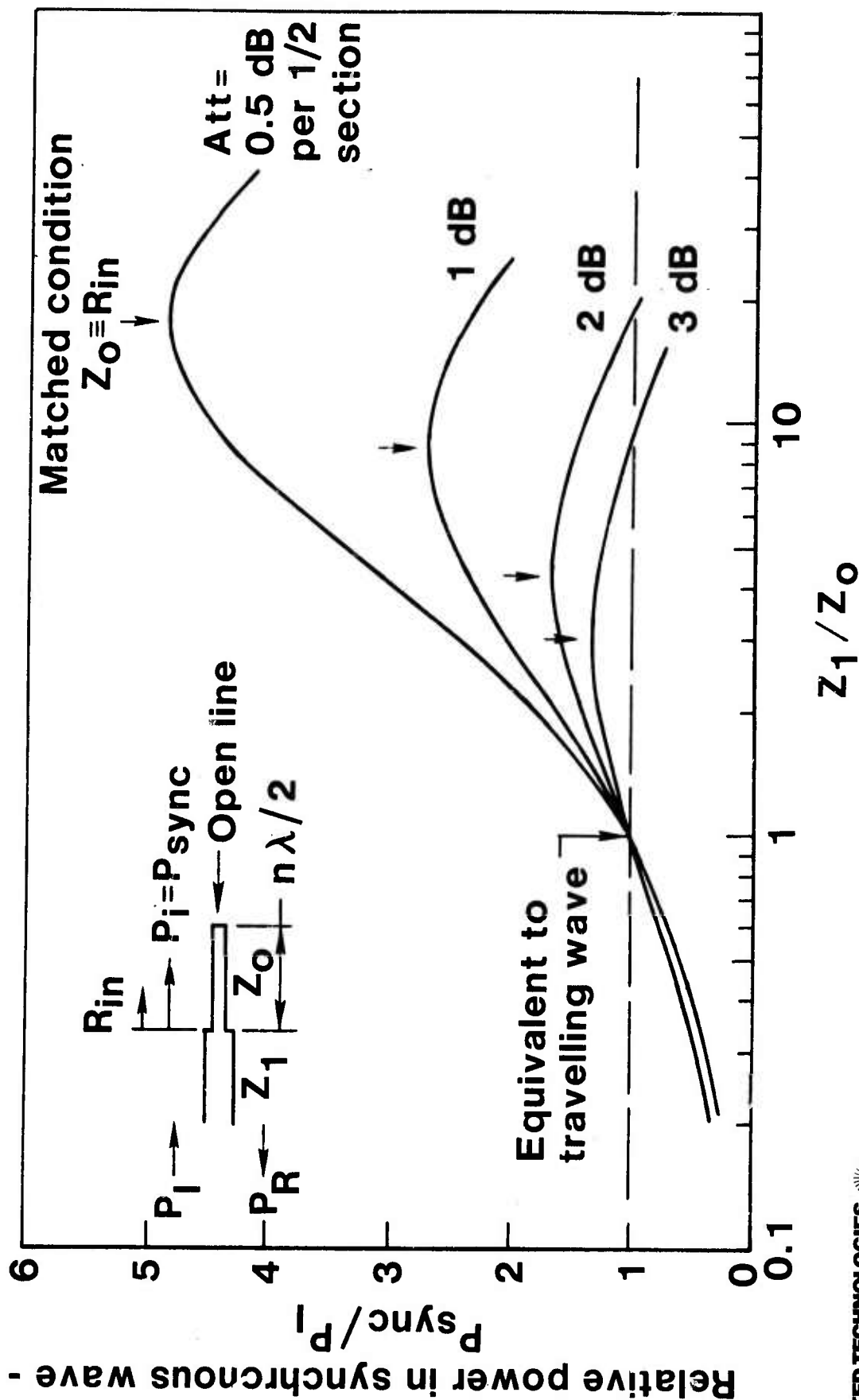
FIG. 5.3

76—03—78—2

THEORETICAL FREQUENCY RESPONSE WITH 2.5Ω SOURCE
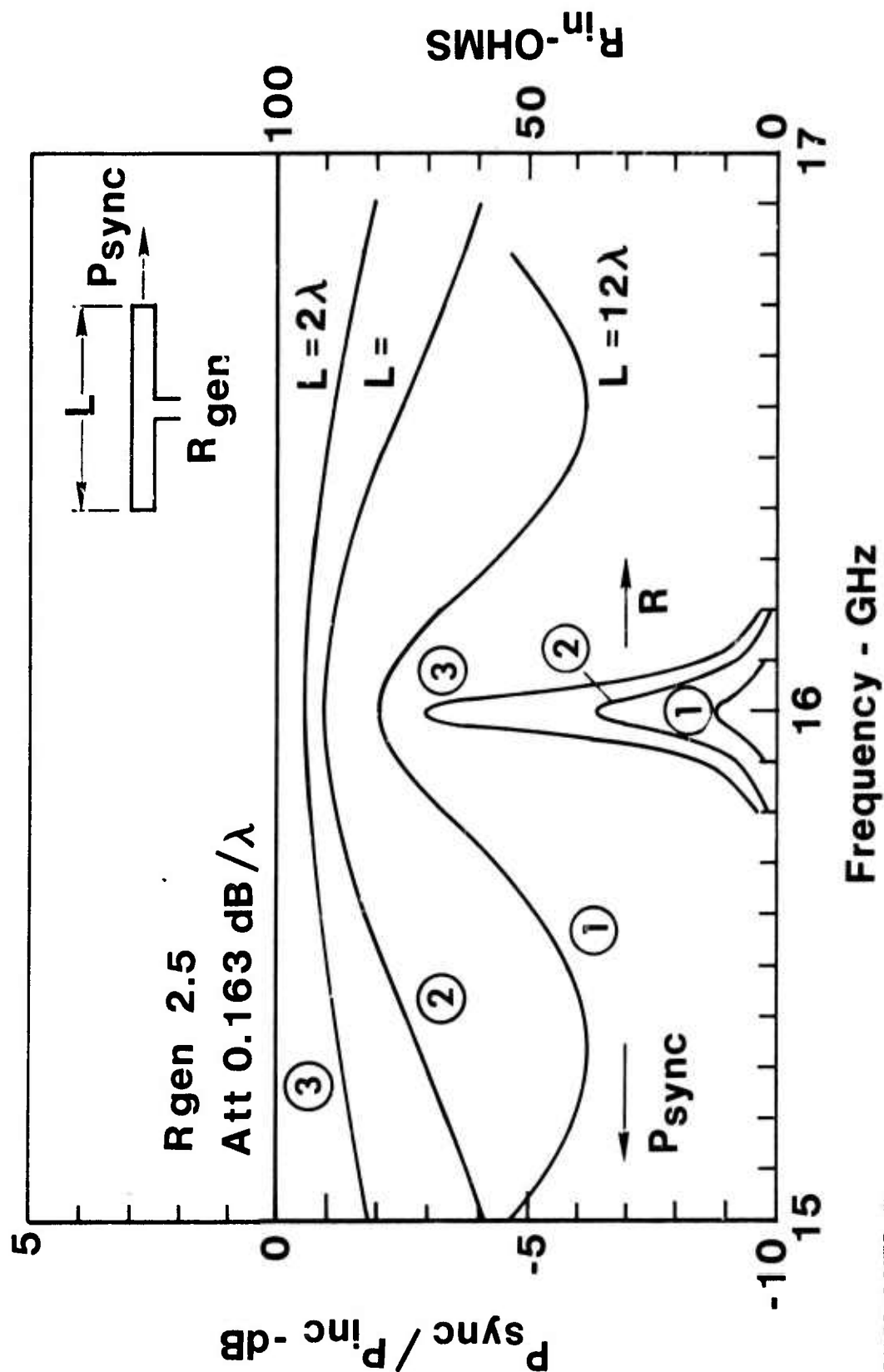
FIG. 5.4

76-03-78-1

5-10

UNITED TECHNOLOGIES
RESEARCH CENTER

THEORETICAL FREQUENCY RESPONSE WITH 10Ω SOURCE

Att 0.163 dB/λ
R Gen = 10Ω

L = 2λ
R = 7.1Ω

L = 4λ
R = 36Ω

L = 12λ
R = 12Ω

P_{sync} / P_{inc} - dB

Frequency - GHz

FIG. 5.5

76-03-78-3

UNITED TECHNOLOGIES
RESEARCH CENTER

5-11
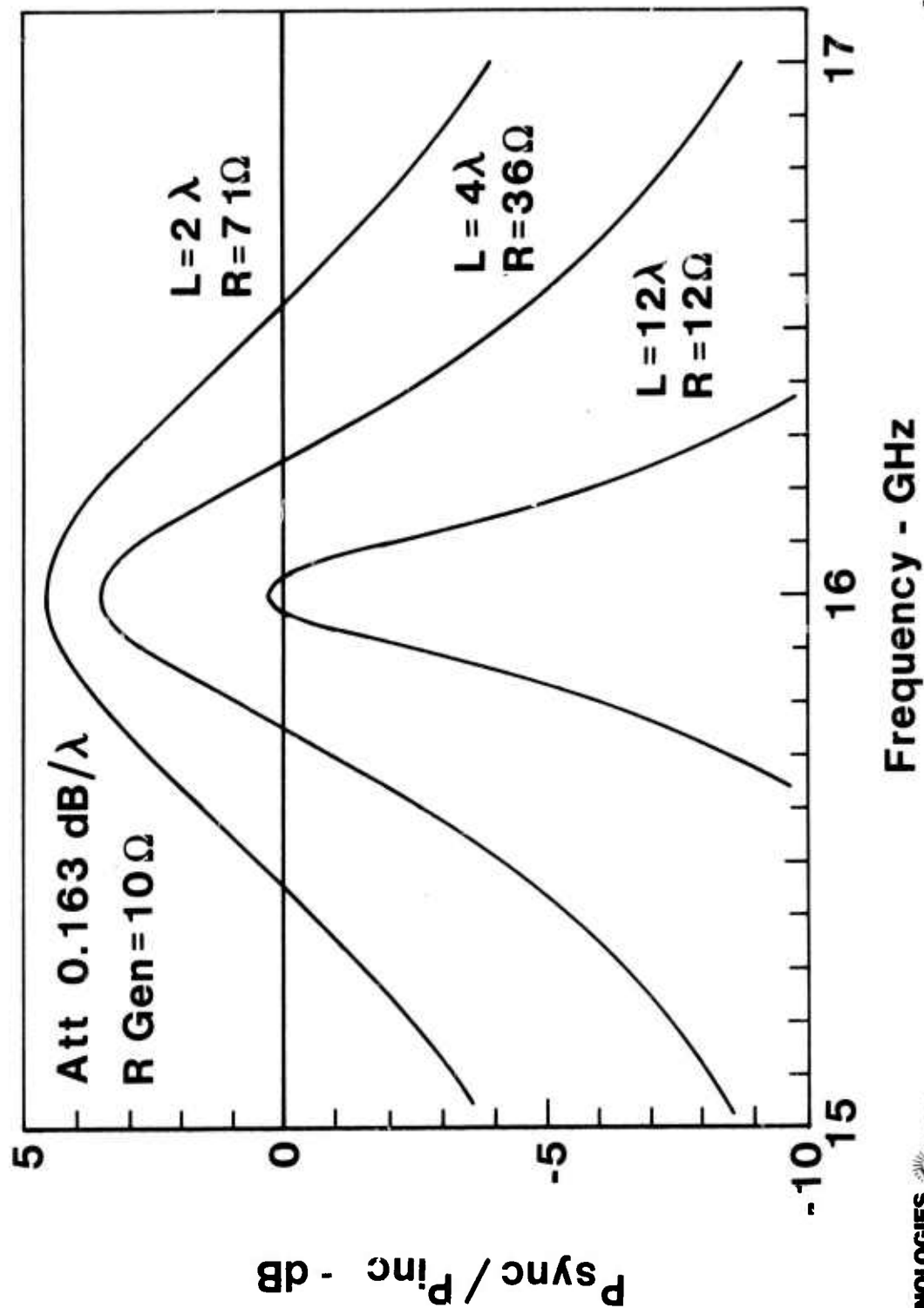
THEORETICAL FREQUENCY RESPONSE WITH IMPEDENCE TRANSFORMERS

FIG. 5.6

76-03-236-1

UNITED TECHNOLOGIES RESEARCH CENTER

5-12
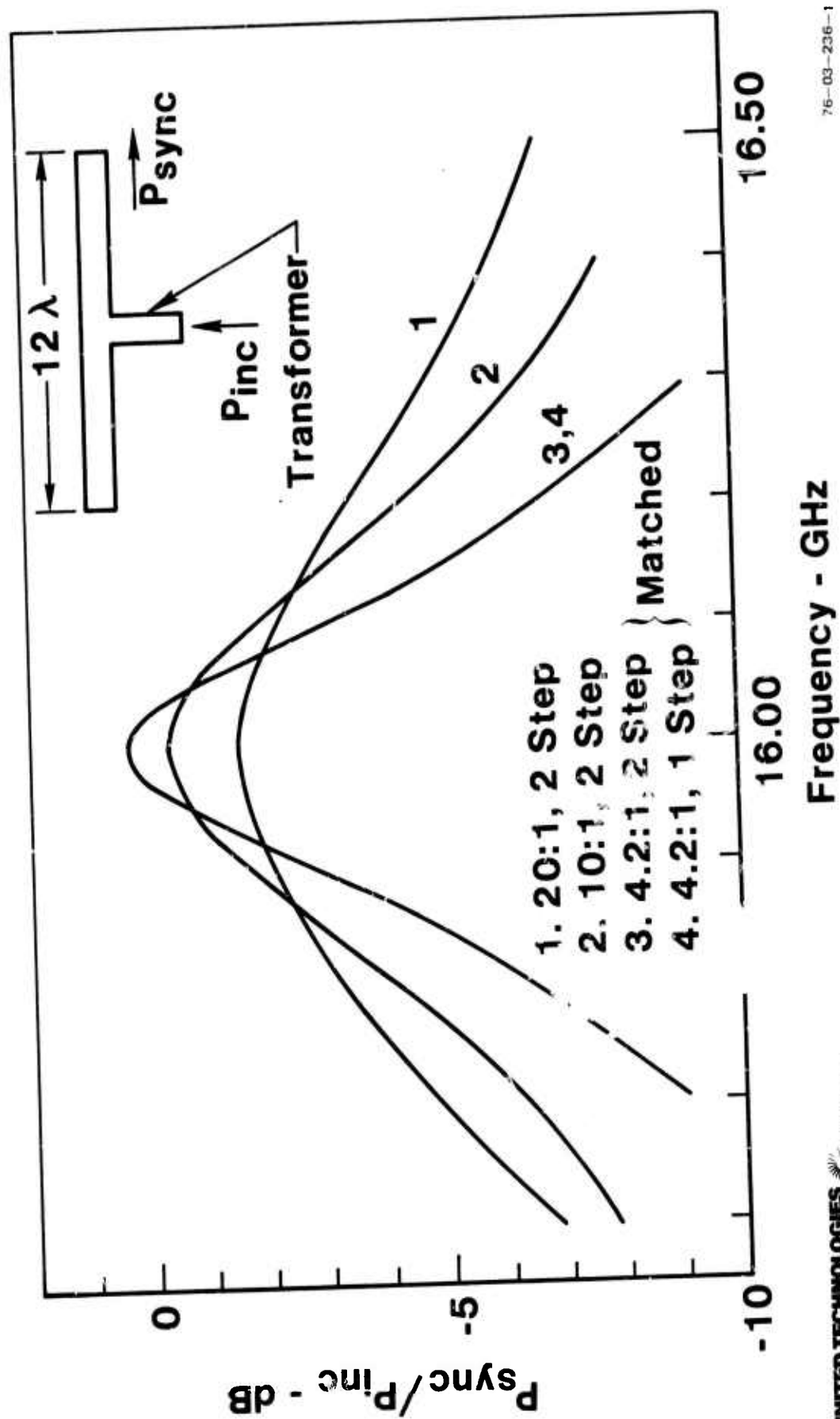
MODULATOR FREQUENCY RESPONSE

FIG. 5.7

76—03—63—5

UNITED TECHNOLOGIES
RESEARCH CENTER

5-13

6.0 OPTICAL AND MICROWAVE MODULATION MEASUREMENTS

6.1 Optical Transmission Characteristics

Optical transmission measurements were made with a CO_2 laser beam of $\approx$ 1 mm in diameter. This constraint is imposed by the m rowave transmission requirement. This rules out the use of grating couplers (1,2) because the optimum coupling length requi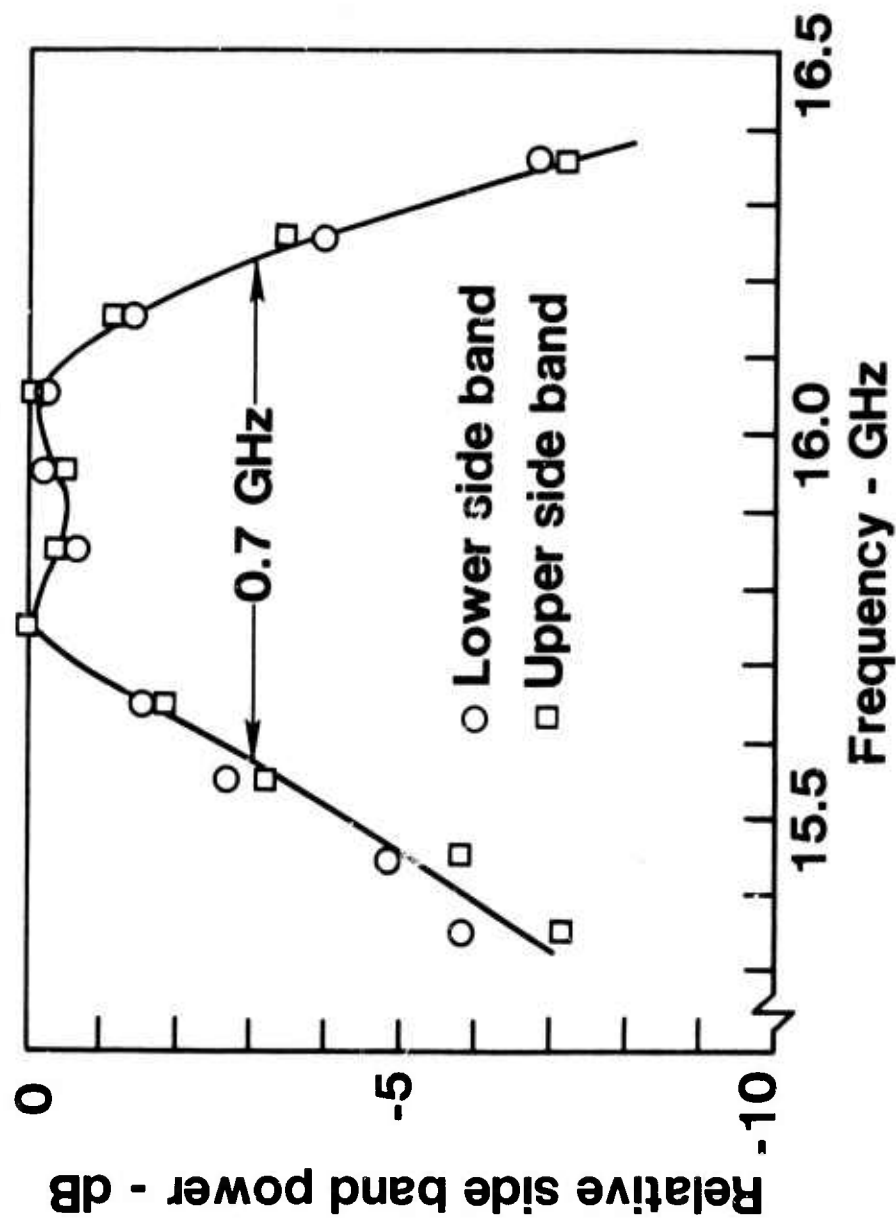red for grating couplers is much gr ter than 1 mm. Results reported here were obtained by using two right-angle germanium prisms with a base area of 5 mm x 5 mm. For better reproducibility, the base of these prisms are optically flat and no attempt was made to create a varying coupling strength by means of a tapered gap spacing. Therefore, the maximum transmission in our case is 81 percent, by assuming a perfect (100 percent) output coupler. All the transmission measurements were made for waveguide thickness ranging from 25 μm, to 35 μm, and for a fixed propagation path length of 2.8 cm. The reason for choosing thicker guides, i.e., 25$\leq$ t $\leq$30 μm, is to eliminate the excessive propagation losses for both the optical (Ref. 3) and the microwave (Ref. 4) power. Previously calculated (Ref. 4) results indicate that the coupling efficiency varies only slowly with the gap spacing, δ, provided that the variations in δ can be kept within 0.1 μm. In practice, this can easily be accomplished by using optically polished prisms and ion-beam thinned waveguides. Transmission measurements through a typical bonded-down GaAs thin-slab waveguide without the top microstrip electrode are shown in Fig. 6.1. For most experiments the input laser power to the waveguides is in the range from 3 to 5 watts and, in some cases, the input laser power has been increased to 15 watts. Optical transmission characteristics remain the same over this range of laser power. Measurements of Fig. 6.1 were made with a Gaussian input laser beam (σ = 0.75 mm). Because of insufficient coupling length, the measured transmission of the TE_0 mode (not shown in Fig. 6.1) was only about 15 percent. The transmission was highest for the TE_1 mode at 46 percent. A sharp reduction in transmitted power for the higher order modes is caused primarily by electrode absorption at the metallic ground plane. To evaluate the power loss at the electrode, a top electrode in a microstrip configuration was subsequently deposited on the surface of the waveguide. The measured transmission for the TE_1 mode propagating in the pressure of both the top and the bottom electrodes over a distance of 2.8 cm was 33 percent. From these two transmission measurements we obtain a value of 0.24 cm^{-1} for the absorption coefficient of the two electrodes for the TE_1 mode. Similarly we obtain a value of 0.05 cm^{-1} for the TE_0 mode. With these values we can estimate the input coupling coefficient from the transmission expression as given by

$$T = 0.92 \, \eta \, \exp \lceil -2.8 \, (\alpha_\ell + \alpha_m) \rceil \tag{1}$$

Equation (1) has taken into account various losses, namely, 1) the loss at two AR coated input and output prism faces, each of which reflects the laser power by about 4 percent, 2) the loss at the input prism with a coupling coefficient η (in all

cases the output prism is assumed to be a perfect coupler), 3) the loss in a single electrode with an absorption coefficient α_ℓ, and 4) the GaAs material absorption coefficient α_m at a known value of 0.01 cm^{-1}. From Eq. (1) we obtain a η value of 17 percent and 72 percent for the TE_0 mode and TE_1 mode, respectively. These values agree very well with our previously (Ref. 4) calculated values.

6.2 Optical Sideband Power Conversion and Modulation Bandwidth

Recent advances in fabrication techniques of the bonded-down GaAs waveguide modulator has led to not only a significant improvement in optical transmission but also to very reproducible microwave impedance characteristics for the microstrip structure. The microstrip structure used in the experiment described below consists of a narrow strip of copper electrode 1 mm wide and 2.8 cm long deposited on the top surface of a 25 μm thick GaAs slab and a copper film deposited over the entire bottom surface of this slab. Microwave power was center-fed into the microstrip through two quarter-wave impedance steps from a 50 ohm coaxial line. This was accomplished by a modification of a commercial connector. The measured effective dielectric constant, attenuation coefficient, and the input impedance for this open-ended circuit at the resonance of 16 GHz were 12.2, 0.75 dB/cm, and 45 ohms, respectively.

Experimental setup for sideband measurements was identical to that used previously (Ref. 5). A well collimated CO_2 laser beam was transmitted through the GaAs waveguide modulator along the (110) plane with its polarization oriented along the ($1\bar{1}0$) plane. The microwave electric field was applied perpendicular to the (001) plane at an estimated rms strength of 3000 volts/cm. The field induced birefringence causes an instantaneous phase shift, $\Delta\phi$, in the guided optical wave at the microwave modulating frequency. A sideband power P_{SB} is generated as a result of phase modulation at the microwave frequency. Figure 6.2 is a photograph of the modulator assembly which is connected to a 22 watts microwave TWT amplifier.

The output which consisted of both laser carrier power P_c and P_{SB}, was analyzed by an electronically scanning Fabry-Perot interferometer, FPI. The mirror spacing of the FPI was set such that each saw-tooth voltage V ramp corresponded to one free-spectral range of 50 GHz. The upper trace of Fig. 6.3 shows the V_{FP} waveform and the lower trace of Fig. 6.3 shows the laser carrier signal and the two sidebands located at ±16 GHz from P_c. The measured conversion efficiency, as defined by

$$P_{SB}/P_c \simeq \frac{1}{4}(\Delta\phi)^2 \tag{2}$$

was found to be $\simeq 1$ percent at 22 watts of imcrowave driving power. This conversion efficiency should increase linearly with increasing driving power. Fig. 6.4 is a plot of the measured P_{SB} as a function of microwave frequency at a constant 22 watts power level. The results indicate that the full modulation bandwidth at the sideband half power points for a standing-wave structure is approximately 1 GHz.

6.3 References

1. Cheo, P. K., D. W. Fradin and R. Wagner: Microwave Waveguide Modulators For CO_2 Lasers, 5th Semi-Annual Technical Report, Contract No. N00014-73-C-0087. March 1975.

2. Fradin, D. W., P. K. Cheo, S. T. Peng and T. Tamir: Integrated Optics Technical Digest, January 12-14, 1976, Paper WD2.

3. Cheo, P. K., J. M. Berak, W. Oshinaky and J. S. Swindal, Appl. Optics, 12, 500 (1973).

4. Cheo, P. K., M. Gilden and R. Wagner: Infrared Waveguide Modulators at Microwave Frequencies, 6th Semi-Annual Technical Report, Contract No. N00014-73-C-0087, September 1975.

5. Cheo, P. K. and M. Gilden, Appl. Phys. Lett., 25, 272 (1974).

OPTICAL TRANSMISSION CHARACTERISTICS

FIG.6.1

Input laser power = 3.5W

Modulator length = 2.8cm

Modulator thickness = 25.5 μm

Transmitted laser power, W

Angle of incidence, deg

TE$_1$

TE$_2$

TE$_3$
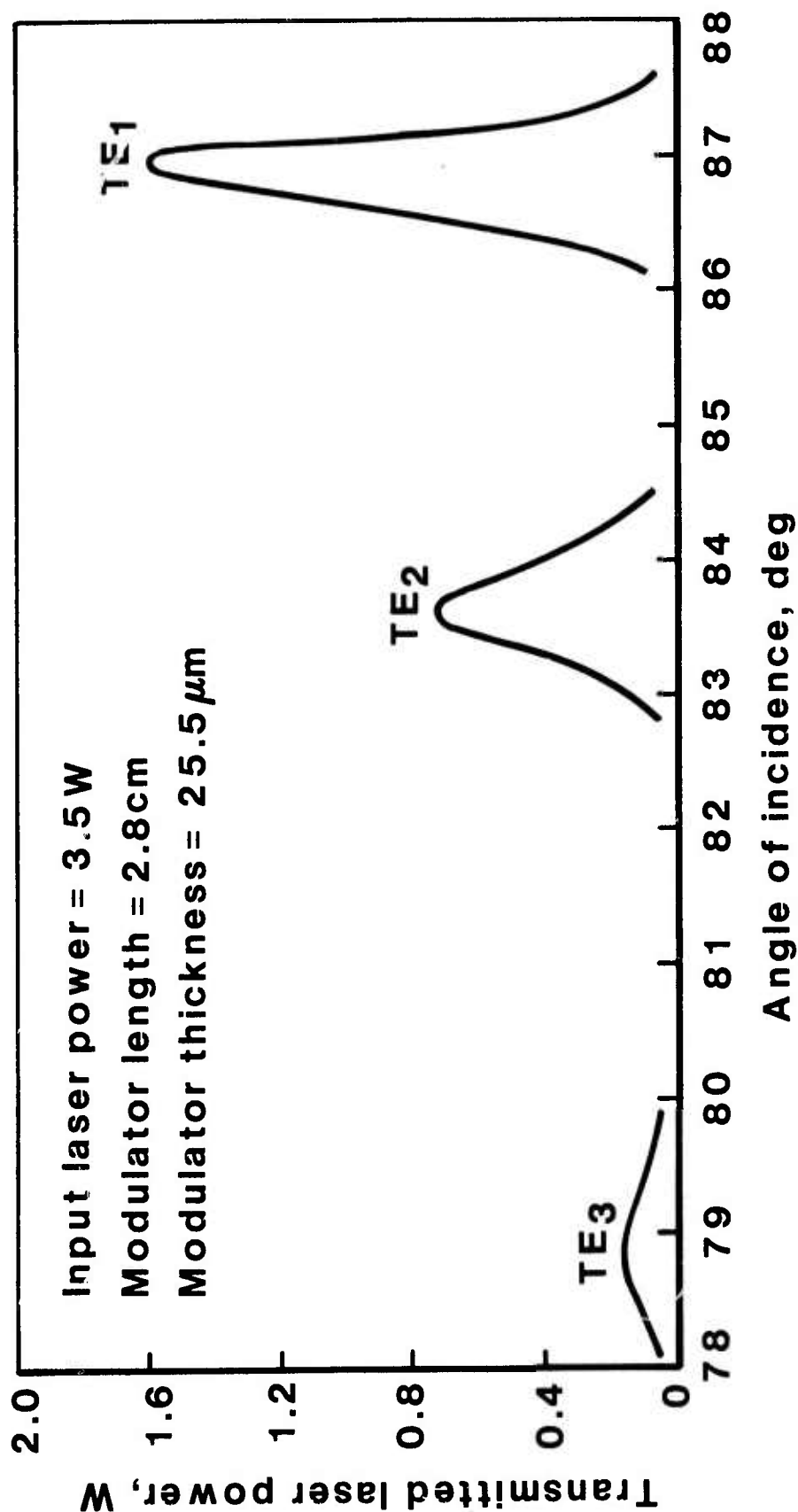
R12-103-1

FIG. 6.2

76-02-211-1

MICROWAVE WAVEGUIDE MODULATOR SYSTEM

FIG. 6.3
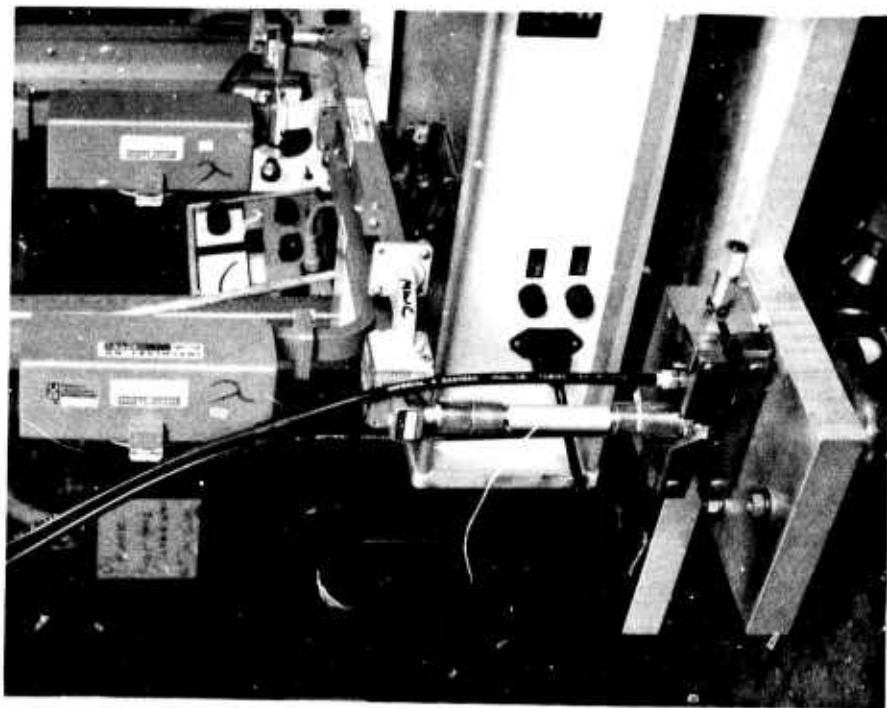
SPECTRAL CHARACTERISTICS OF A MODULATED CO_2 LASER

$P_{SB} \simeq 40 mW$

$P_C = 4 W$

16GHz

V_{FP}
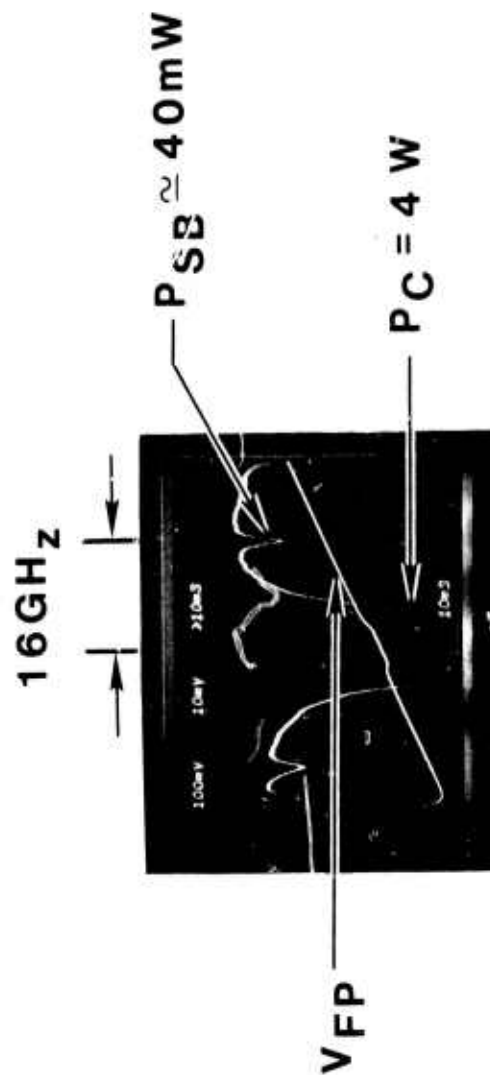
MEASURED SIDEBAND POWER CONVERSION EFFICIENCY VS MICROWAVE FREQUENCY
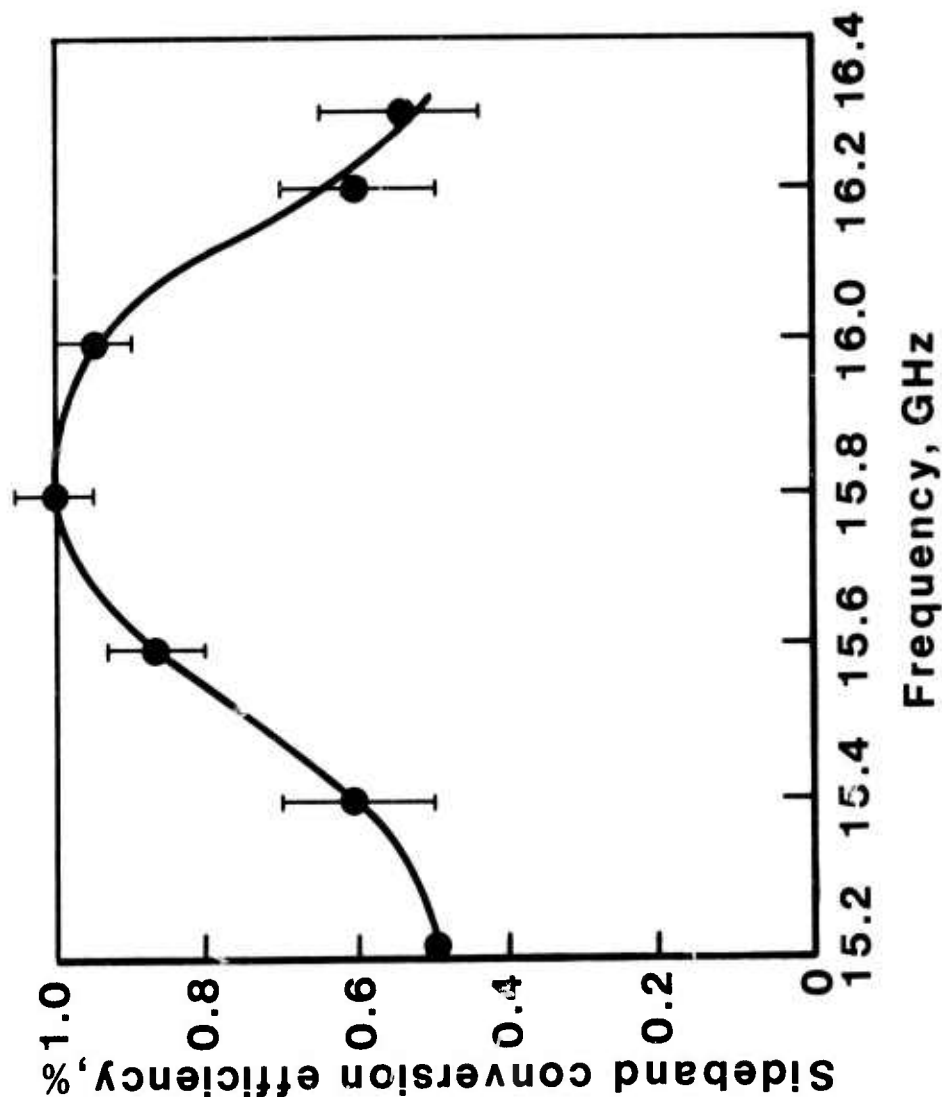
FIG. 6.4

7.0   CHANNEL WAVEGUIDES

7.1   Introduction

The quality of the transmitted laser beam through the waveguide depends strongly on not only the quality of the waveguide and the couplers but also the electrode configuration. Of particular importance is the stress-induced birefringence along the edge of a microstrip electrode, that can cause beam distortion in the X direction (Fig. 7.1). Nearly perfect beam shape has been obtained with these bonded-down planar waveguides in the absence of the top electrode. When a top electrode in the form of a microstrip line (1 mm x 2.8 cm) is deposited on the surface of a bonded thin-slab GaAs waveguide, the transmitted laser beam shape is severely distorted, as indicated in Fig. 7.1 for an incident beam size of $\approx$ 0.7 mm, propagating underneath the electrode. The output beam quality is restored if the propagation path is outside the electrode region. The elliptical output becomes asymmetric if the confocal beam is slightly misaligned with respect to the electrode. The elliptical distortion increases further with applied microwave power. We attribute the cause of the above observed lens-like effect to a stress-induced birefringence along the edge of the electrode. Because of the electrode geometry, it is very difficult to achieve a perfect alignment. A diffraction-limited beam can only be collimated within the narrow microstrip with its width to length ratio, d/L, as given by (Ref. 1)

$$d^2/L \geq 36 \; \lambda/n\pi$$

where λ and n are the laser wavelength and refractive index, respectively. For a width of 1 mm, the length can not exceed 3 cm.

This section introduces an optimum waveguide structure which shall not only remove the beam distortion problem but also shall improve the optical transmission. We have already demonstrated the former by using a simple channel waveguide. Work is in progress to develop an advanced waveguide structure which can provide both features as mentioned above.

7.2   Channel and Raised Ridge Structures

Experimentally, we found that this lens-like effect can be eliminated by increasing the electrode width from 1 mm to 2 mm for an input beam size of $\sigma \leq$ 1 mm. From the modulator design point of view, this is not desirable because an increase in electrode area causes an increase in the device capacitance or a decrease in effective impedance and also reduces the power density of the modulator driver. A more desirable approach is to compensate the difference in refractive index along the edges of the electrode by removing a small amount of GaAs material to form a simple

channel waveguide, as shown in Fig. 7.2 (a). With a simple channel waveguide, we have obtained the desired beam confinement within an one millimeter wide channel in the presence of microstrip electrode. The transmitted laser beam shapes through a 25 μm thick and 1 mm wide channel waveguide with a channel depth of $\sim$ 5 μm are shown in Fig. 7.3. Figure 7.3 (a) depicts the input beam shape. Figure 7.3 (b) shows the output beam shape when a TE_1 mode is launched from the point A as indicated in Fig. 7.2 (a). Two finite steps in the waveguide do not cause any discernable beam distortion but only cause a slight decrease in the transmitted power as compared with that transmitted through the channel. Figure 7.3 (c) shows the output beam shape when a TE_1 mode is launched from the Point C, as indicated in Fig. 7.2 (a), which is located in the center of the channel. In this case, the top surface of this channel is coated with a 10 μm thick copper film. As the out-coupled beam emerges from this narrow channel with a width D - 1 mm, it spreads slightly, as shown in Fig. 7.3 (c), at a diffraction angle, $2\lambda/D$, of about 0.02 radians. If the laser is incident at the point B which is located at the edge of the channel, the output splits into two beams as shown in 7.3(d). In some cases, a splitting into a multiple spots can also occur if the direction of propagation is not in perfect alignment with the edge.

A simple channel waveguide with a channel length of 2.8 cm has been used in an experiment with a TEM_{00} mode CO_2 laser at the P(20), $00^00 1 - 10^0 0$ V-R transition. At 12 watts input laser power level, we obtained a transmitted power of 4 watts via a coupling of the TE_1 mode. The total power loss in the transmission is 8 watts, of which approximately one half is lost at input coupler and the other half is lost in the electrodes. To recover some of these losses, we have considered the case of a slowly tapered raise-ridge waveguide structure, as shown in Fig. 7.2(b). The advantages of using such type a structure are: 1) to improve coupling efficiency for the TE_0 mode for small input beam sizes, 2) to reduce the propagation loss, 3) to increase the driving power density by narrowing the ridge width. If the ridge height is at 25 μm, the power loss due to the absorption of the 2.8 cm long electrodes for the TE_0 mode is only about 13 percent, which is calculated by using the data from Ref. 2. However, the waveguide thickness in the coupling region must be decreased by a substantial amount in order to efficiently excite the TE_0 mode.

The input prism coupling efficiency for the TE_0 mode and the TE_1 mode as a function of waveguide thickness are presented in Fig. 7.4 and 7.5. These η-values are calculated by using the formulations of Tien and Ulrich (Ref. 3). In all cases, the coupling air gap-spacing has been chosen to be 0.1 μm, a value which can easily be achieved in practice. For values of σ in the range of 0.5 to 1 mm, the optimum coupling of TE_0 mode occur at waveguide thickness in the neighborhood of 10 to 13 μm (Fig. 7.4), which is about 0.6 times that of the optimum thickness for coupling of the TE_1 mode (Fig. 7.5).

These results indicate that it is possible to excite efficiently the lowest loss guided-wave mode (TE_0) of a 10 microns thick GaAs waveguide with a focused CO_2 laser beam of the size less than or equal to 0.5 mm in diameter. This guided-wave mode will subsequently be propagated into a slowly tapered raised-ridge channel with a slight increase in B/k value ($\Delta\beta/k \approx 0.025$). The energy will be confined within this channel over a long propagation length. Because of low electrode absorption loss ($2\alpha_e = 0.05$ cm^{-1}), a transmission of 67 percent of the incident laser power is expected for a 3 cm long metal-cladded thin-slab waveguide modulator. Work is in progress to verify this prediction.

7.3 References

1. Kausinow, I. P. and E. H. Turner, Proc. IEEE, 54, 1374 (1966).

2. Cheo, P. K., J. M. Berak, W. Oshinsky and J. L. Swindal, Appl. Optics, 12, 500 (1973).

3. Tieu, P. K. and R. Ulrich, J. Opt. Soc. Am., 60, 1325 (1970).

EFFECT OF ELECTRODE ON A GUIDED MODE

FIG. 7.1

Output beam

Gaussion

Distorted

z

y

x

L

d
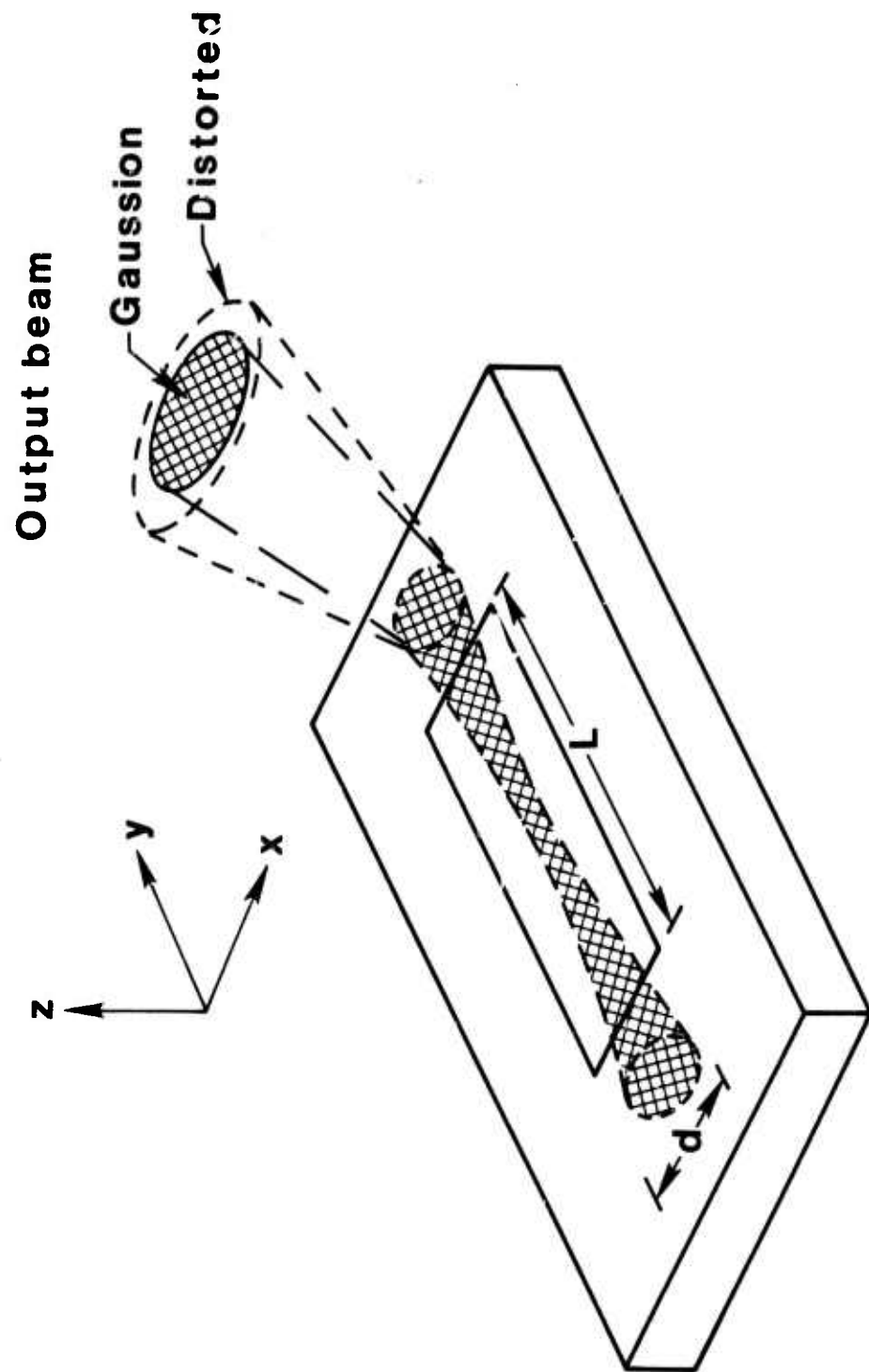
FIG. 7.2

CHANNEL WAVEGUIDES

a) Simple channel
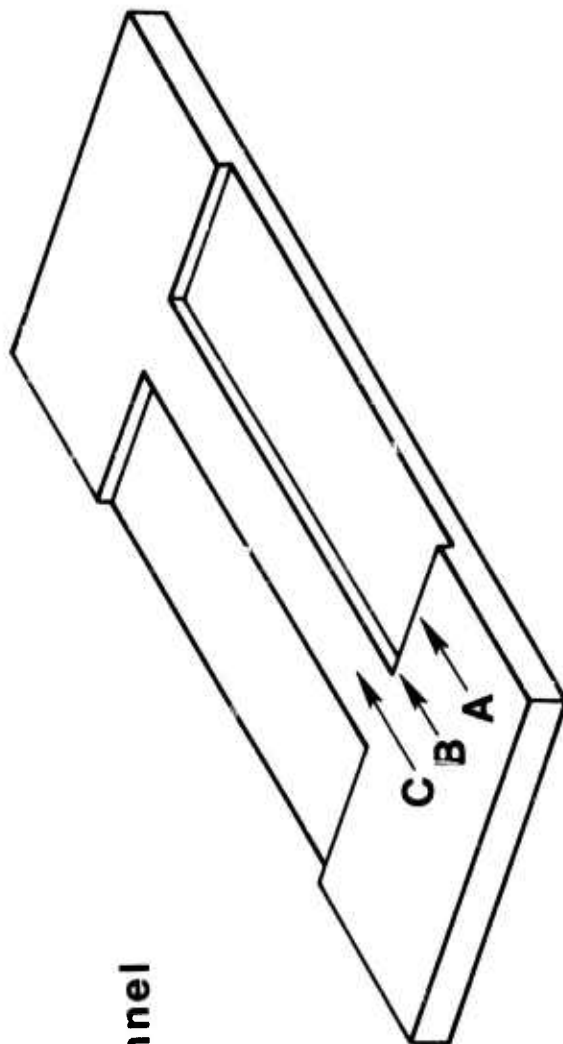
b) Slowly tapered, raise ridge channel

FIG. 7.3
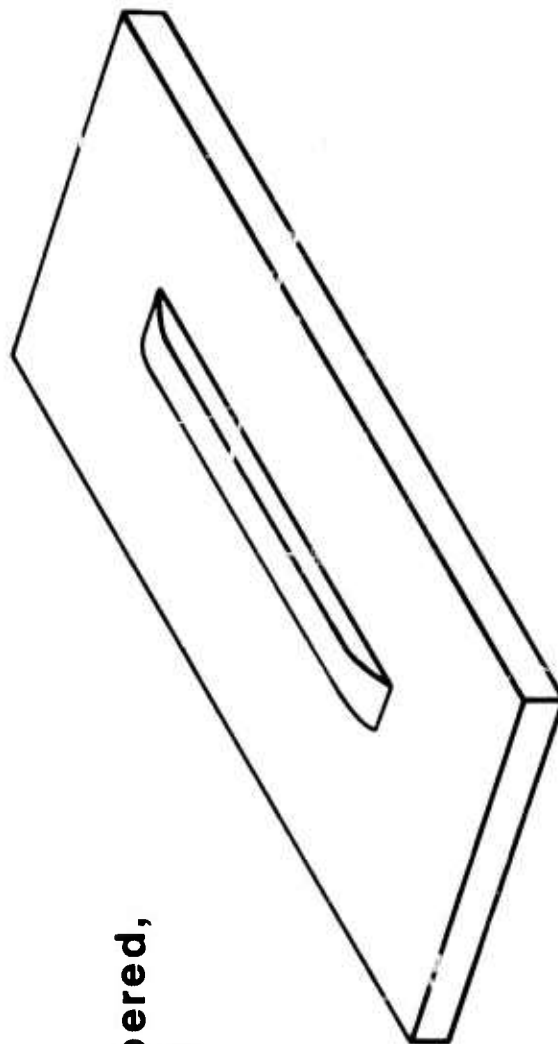
LASER BEAM SHAPES

(a)   (b)   (c)   (d)

76—02—205— 1
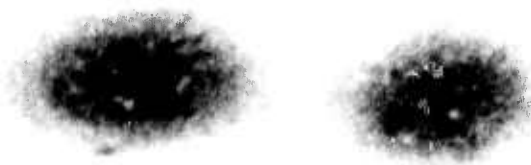
PRISM COUPLING EFFICIENCY FOR TE₀ MODE

FIG. 7.4

TE₀ mode

$\delta = 0.1 \mu m$

Input prism coupling efficiency, η

Waveguide thickness, microns

σ, mm
0.5
0.75
1.0
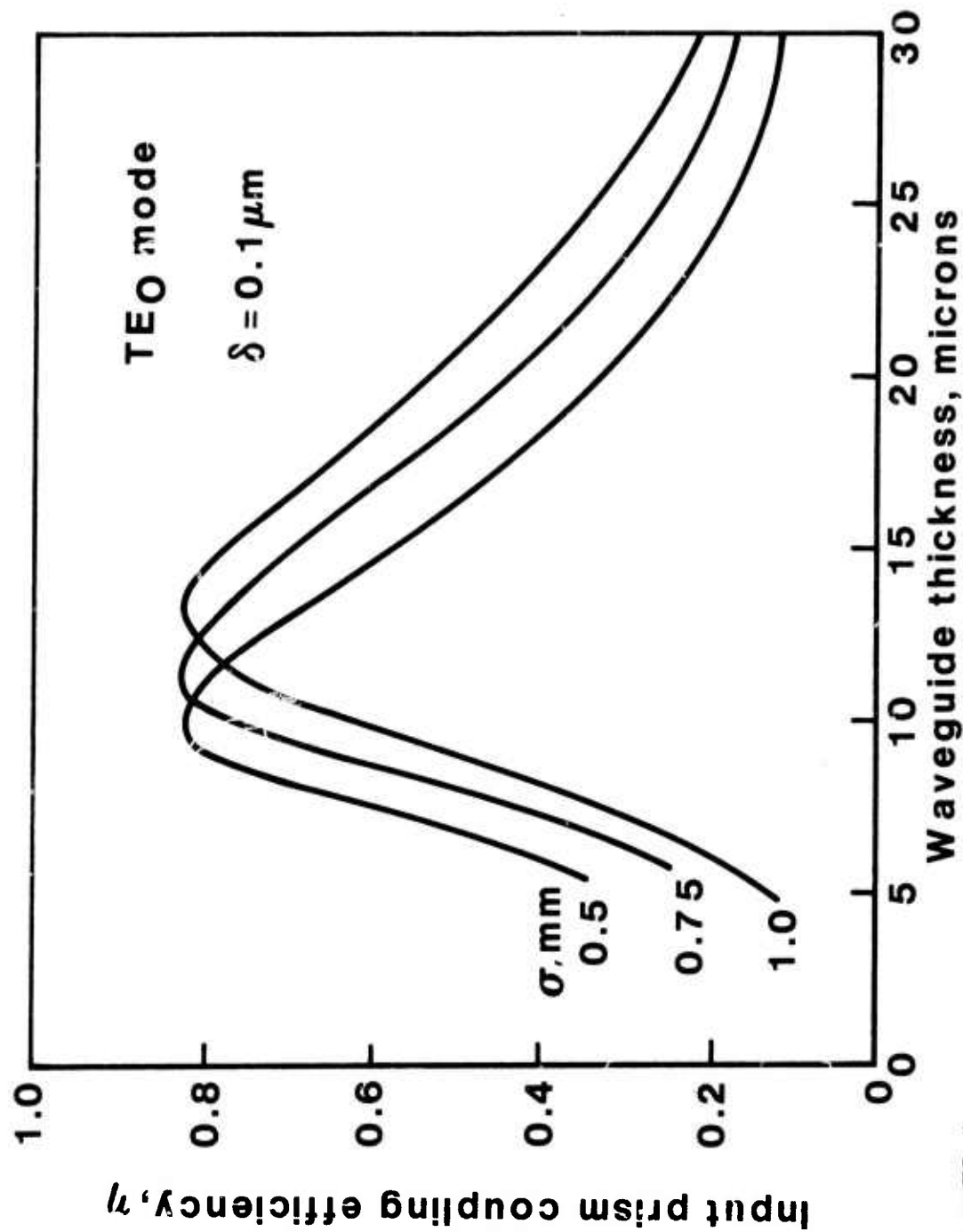
76–02–196–4

PRISM COUPLING EFFICIENCY FOR TE₁ MODE

FIG. 7.5

76—02—196—3

TE$_1$ mode
$\delta = 0.1\ \mu m$

σ, mm
0.5
0.75
1.0

Waveguide thickness, microns

Input prism coupling efficiency, η

UNITED TECHNOLOGIES
RESEARCH CENTER

7-8

Office of Naval Research Branch Office   1 copy
Attn: Dr. Robert Behringer
1030 East Green Street
Pasadena, California 91106

Code 102 1P (ONRL)   6 copies
Office of Naval Research
800 N. Quincy Street
Arlington, Virginia 22217

Defense Advanced Research Projects Agency   2 copies
1400 Wilson Blvd.
Arlington, Virginia 22209
Attn: Director, Laser Division
       Dr. P. Clark

ODDR&E   1 copy
Pentagon
Washington, D. C. 20301
Attn: Ass't. Dir. (Space and Advanced Systems)   1 copy

Office of the Ass't Secretary of Defense   1 copy
System Analysis (Strategic Programs)
Washington, D. C. 20301
Attn: Mr. Gerald R. McNichols

U.S. Arms Control and Disarmament Agency   1 copy
Dept. of State Bldg., RM 4931
Washington, D. C. 20451
Attn: Dr. Charles Henkin

Energy Research Development Agency   1 copy
Division of Military Applications
Washington, D. C. 20545

National Aeronautics and Space Administration   1 copy
Lewis Research Center
Cleveland, Ohio 44135
Attn: Dr. John W. Dunning, Jr.
       (Aerospace Res. Engineer)

National Aeronautics & Space Administration   1 copy
Code RR, FOB 10B
600 Independence Ave. SW
Washington, D. C. 20546

National Aeronautics and Space Administration
Ames Research Center
Moffet Field, California 94035
Attn: Mr. Robert L. McKenzie   1 copy
       Dr. Kenneth W. Billman   1 copy

Department of the Army
Office of the Chief of RD&A
Washington, D. C. 20310
Attn: DARD-DD   1 copy
       DAMA-WSM-T   1 copy

Department of the Army   2 copies
Office of the Deputy Chief of Staff
  for Operations & Plans
Washington, D. C. 20310
Attn: DAMO-RQD

Ballistic Missile Defense Program Office (BMDPO)   3 copies
The Commonwealth Bldg.
1300 Wilson Blvd.
Arlington, Virginia 22209
Attn: Mr. Albert J. Bast, Jr.

U. S. Army Missile Command   2 copies
Research and Development Division
Redstone Arsenal, Alabama 35809
Attn: Army High Laser Energy Programs

Commander   1 copy
Rock Island Arsenal
Rock Island, Illinois 61201
Attn: SARRI-LR, Mr. J. W. McGarvey

Commanding Officer   1 copy
U.S. Army Mobility Equipment R&D Center
Ft. Belvior, Virginia 22060
Attn: SMEFB-MV

Commander   1 copy
U. S. Army Armament Command
Attn: AMSAR-RDT
Rock Island, Illinois 61201

Director
Ballistic Missile Defense Advanced Technology Center
P. O. Box 1500
Juntsville, Alabama   35807
Attn: ATC-C   1 copy
        ACT-T   1 copy

Commander
U. S. Army Material Command
Alexandria, Virginia   22304
Attn: Mr. Paul Chernoff (AMCRD-T)   1 copy
        Dr. B. Zarwyn (AMCRD-T)   1 copy

Commanding General   1 copy
U. S. Army Nunitions Command
Dover, New Hampshire   07801
Attn: Mr. Gilbert F. Chesnov (AMSMU-R)

Director
U. S. Army Ballistic Res. Lab
Aberdeen Proving Ground, MD 21005
Attn: Dr. Robert Eichelberger   1 copy
        Mr. Frank Allen   1 copy
        Dr. E. C. Alcarez   1 copy

Commandant
U. S. Army
Air Defense School
Ft. Bliss, Texas   79916
Attn: Air Defense Agency   1 copy
        ATSA-CTD-MS   1 copy

Commanding General
U. S. Army Combat Dev. Command
Ft. Belvoir, Virginia   22060
Attn: Director of Material, Missile Div.   1 copy

Commander   1 copy
U. S. Army Training And Doctrine Command
Attn: ATCD-CF
Ft. Monroe, Virginia   23651

Commander   1 copy
U. S. Army Frankford Arsenal
Philadelphia, Pennsylvania   19137
Attn: Mr. M. Elnick SARFA-FCD
        Bldg. 201-3

Commander   1 copy
U. S. Army Electronics Command
Ft. Monmouth, New Jersey 07703
Attn: AMSEL-CT-L, Dr. R. G. Buser

Commander   1 copy
U. S. Army Combined Arms Combat
 Developments Activity
Ft. Leavenworth, Kansas 66027

National Security Agency   1 copy
Ft. Geo. G. Meade, Maryland 20755
Attn: R. C. Foss A763

Deputy Commandant for Combat &   1 copy
 Training Developments
U. S. Army Ordnance Center and School
Attn: ATSL-CTD-MS-R
Aberdeen Proving Ground, Maryland 21005

Commanding Officer   1 copy
USACDC CBR Agency
Ft. McClellan, Alabama 36201
Attn: CDCCBR-MR (Mr. F. D. Poer)

Department of the Navy   1 copy
Office of the Chief of Naval Operations
Pentagon 5C739
Washington, D. C. 20350
Attn: (OP 9b2F3)

Office of Naval Research
Attn: Dr. Fred Quelle   1 copy
       Dr. M. White   1 copy
495 Summer Street
Boston, Massachusetts 02210

Department of the Navy   1 copy
Deputy Chief of Naval Material (Dev.
Washington, D. C. 20360
Attn: Mr. R. Gaylord (MAT 032B)

Naval Missile Center
Point Mugu, California 93042
Attn: Gary Gibbs (Cod. 5352)   1 copy

Naval Research Lab
Washington, D. C. 20375
Attn: (Code 5503-LTPO)
        Dr. P. Livingston   (Code 55060)   1 copy
        Dr. A. I. Schindler (Code 6330)   1 copy
        Dr. H. Shenker   (Code 6530)   1 copy
        Mr. D. J. McLaughlin(Code 5560)   1 copy
        Dr. Jonn L. Walsh   (Code 5503)   1 copy

High Energy Laser Project Office   1 copy
Department of the Navy
Naval Sea Systems Command
Washington, D. C. 20360
Attn: Capt. J. G. Wilson, USN (PMS-405)

Superintendent   1 copy
Naval Postgraduate School
Monterey, California 93940
Attn: Library (Code 2124)

Navy Radiation Technology Liaison Office   1 copy   .
Air Force Weapons Lab. (NLO)
Kirtland AFB, New Mexico 87117

Naval Surface Weapons Center
White Oak
Silver Spring, Maryland 20910
Attn: Dr. Leon H. Schindel (Code 310)   1 copy
        Dr. E. Leroy Harris (Code 313)   1 copy
        Mr. K. Enkenhus   (Code 034)   1 copy
        Mr. J. Wise   (Code 047)   1 copy

U. S. Naval Weapons Center
China Lake, California 93555
Attn: (Code 5114)   1 copy
        Technical Library   1 copy

HQ USAF (AF/RDFS)   1 copy
Pentagon
Washington, D. C. 20330
Attn: Lt. Col. A. J. Chiota

HQ AFSC/XRLW   1 copy
Andrews AFB
Washington, D. C. 20331
Attn: Maj. J. M. Walton

```
HQ AFSC (DLCAW)                                      1 copy
Andrews AFB
Washington, D. C.  20331
Attn:  Maj. H. Axelrod


Air Force Weapons Lab
Kirtland AFB, New Mexico  87117
Attn:  LR                                           4 copies
       AL                                           2 copies


HQ SAMSO (SRTD)
P. O. Box 92960, Worldway Postal Center
Los Angeles, California  90009
Attn:  Lt. Dorian DeMaio (XRTD)                     1 copy


AF Avionics Lab (TEO)
Wright Patterson AFB, Ohio  45433
Attn:  Mr. K. Hutchinson                            1 copy


Dept. of the Air Force
Air Force Materials Lab. (AFSC)
Wright Patterson AFB, Ohio  45433
Attn:  Maj. Paul Elder (LPS)
       Laser Window Group                           1 copy


HQ Aeronautical Systems Division
Wright Patterson AFB, Ohio  45433
Attn:  XRF - Mr. Clifford Fawcett                   1 copy


Rome Air Development Command
Griffiss AFB
Rome, New York  13440
Attn:  Mr. R. Urtz  (OCSE)                          1 copy


HQ Electronics Systems Div. (ESL)
L. G. Hanscom Field
Bedford, Massachusetts  01730
Attn:  Mr. Alfred E. Anderson (XRT)                 1 copy
       Capt. James C. Jalbert (XRJ)                 1 copy
       Technical Library                            1 copy


Air Force Rocket Propulsion Lab
Edwards AFB, California  93523
Attn:  B. R. Bornhorst, (LKCG)                      1 copy
```

Air Force Aero Propulsion Lab   1 copy
Wright Patterson AFB, Ohio 45433
Attn: Col. Walter Moe (CC)

Dept. of the Air Force
Foreign Technology Division
Wright Patterson AFB, Ohio 45433
Attn: PDTN   1 copy

CINCSAC/INEP
Offutt AFB, Nebraska 66113   1 copy

Commandant of the Marine Corps.
Scientific Advisor (Code RD-1)
Washington, D. C. 20380   1 copy

USAF/INANA
Washington, D. C. 20330
Attn: Lt. Col. W. M. Truesdell   1 copy

Aerospace Research Labs., (AP)
Wright Patterson AFB, Ohio 45433
Attn: Lt. Col. Max Duggins   1 copy

Defense Intelligence Agency
Washington, D. C. 20301
Attn: Mr. Seymour Berler (DTIB)   1 copy

Central Intelligence Agency
Washington, D. C. 20505
Attn: Mr. Julian C. Nall   1 copy

Analytic Services, Inc.   1 copy
5613 Leesburg Pike
Falls Church, Virginia 22041
Attn: Dr. John Davis

Aerospace Corp.
P. O. Box 92957
Los Angeles, California 90009
Attn: Dr. G. P. Millburn   1 copy

Massachusetts Institute of Technology
Lincoln Lab - P. O. Box 73
Lexington, Massachusetts 02173
Att: Dr. R. Kingston   1 copy
      Dr. P. Ingwersen   1 copy
      Dr. L. Tomasetta   1 copy